The Near Infrared Spectral Energy Distribution of Young Star Clusters in the FEAST Galaxies: Missing Ingredients at 1–5 μm

Alex Pedrini[1] , Angela Adamo[1] , Arjan Bik[1] , Daniela Calzetti[2] , Sean T. Linden[3] , Benjamin Gregg[2] , Varun Bajaj[4] ,
Jenna E. Ryon[4] , Anne S. M. Buckner[5] , Giacomo Bortolini[1] , Michele Cignoni[6,7,8] , Matteo Correnti[9,10] ,
Ana Duarte-Cabral[5] , Bruce G. Elmegreen[11] , Helena Faustino Vieira[1] , John S. Gallagher[12] , Kathryn Grasha[13,14,20] ,
Kelsey E. Johnson[15] , Mark R. Krumholz[16] , Drew Lapeer[2] , Thomas S.-Y. Lai[17] , Matteo Messa[18] , Göran Östlin[1] ,
Linn Roos[19] , Linda J. Smith[4] , and Monica Tosi[7]

[1] Department of Astronomy, Oskar Klein center, Stockholm University, AlbaNova University center, SE-106 91 Stockholm, Sweden; alex.pedrini@astro.su.se
[2] Department of Astronomy, University of Massachusetts, 710 North Pleasant Street, Amherst, MA 01003, USA
[3] Steward Observatory, University of Arizona, 933 N Cherry Avenue, Tucson, AZ 85721, USA
[4] Space Telescope Science Institute, 3700 San Martin Drive, Baltimore, MD 21218, USA
[5] Cardiff Hub for Astrophysics Research and Technology (CHART), School of Physics & Astronomy, Cardiff University, The Parade, CF24 3AA Cardiff, UK
[6] Dipartimento di Fisica, Università di Pisa, Largo Bruno Pontecorvo 3, 56127, Pisa, Italy
[7] INAF—Osservatorio di Astrofisica e Scienza dello Spazio di Bologna, via Piero Gobetti 93/3, 40129 Bologna, Italy
[8] INFN, Largo B. Pontecorvo 3, 56127, Pisa, Italy
[9] INAF Osservatorio Astronomico di Roma, Via Frascati 33, 00078, Monteporzio Catone, Rome, Italy
[10] ASI-Space Science Data Center, Via del Politecnico, I-00133, Rome, Italy
[11] Katonah, NY 10536, USA
[12] Department of Astronomy, University of Wisconsin-Madison, 475 N. Charter Street, Madison, WI 53706, USA
[13] Research School of Astronomy and Astrophysics, Australian National University, Canberra, ACT 2611, Australia
[14] ARC Centre of Excellence for All Sky Astrophysics in 3 Dimensions (ASTRO 3D), Australia
[15] Department of Astronomy, University of Virginia, Charlottesville, VA 22904, USA
[16] Research School of Astronomy & Astrophysics, Australian National University, 233 Mt Stromlo Rd, Stromlo, ACT 2611, Australia
[17] IPAC, California Institute of Technology, 1200 E. California Blvd., Pasadena, CA 91125, USA
[18] INAF—OAS, Osservatorio di Astrofisica e Scienza dello Spazio di Bologna, via Gobetti 93/3, I-40129 Bologna, Italy
[19] Department of Physics and Astronomy, Uppsala University, Box 516, SE-751 20 Uppsala, Sweden

Abstract

We present a combined Hubble Space Telescope (HST) and JWST 0.2–to–5 μm analysis of the spectral energy distributions (SED) of emerging young star clusters (eYSCs) in four nearby galaxies from the Feedback in Emerging Extrgalactic Star Clusters survey: M51, M83, NGC 628, and NGC 4449. These clusters, selected for their bright Paα and 3.3 μm polycyclic aromatic hydrocarbon emission, are still associated with their natal gas cloud and have been largely missed in previous HST optical campaigns. We modeled their SEDs using the CIGALE fitting code and identified (i) a systematic flux excess at 1.5–2.5 μm that is not accounted for by current stellar population models and (ii) the preference for a set of dust model parameters that is not aligned with expectations from self-consistent analyses of star-forming regions, suggesting model shortcomings also in the 3–5 μm. The near-infrared excess is most prominent in low-mass ($\leqslant 3000\,M_{\odot}$) and young ($\leqslant 6$ Myr) clusters. Additionally, we see that the SED fitting analysis wrongly assigns ages $\geqslant 6$ Myr to a fraction of strong Paα emitters with equivalent widths suggestive of significantly younger ages. A parallel analysis with the `slug` code suggests that stochastic initial mass function (IMF) sampling of pre-main-sequence stars combined with extinction might partially reduce the gap. We conclude that the inclusion of young stellar object SEDs, along with more realistic sampling of the cluster IMF, might be needed to fully account for the stellar population and dust properties of eYSCs.

Unified Astronomy Thesaurus concepts: Star clusters (1567); Polycyclic aromatic hydrocarbons (1280); Star formation (1569); Spectral energy distribution (2129); Galaxies (573)

1. Introduction

The appearance and evolution of galaxies are largely governed by their star formation activity. Due to its hierarchical nature (B. G. Elmegreen & Y. N. Efremov 1996), star formation is linked to the presence of clustered structures. At parsec scales, thousands of young star clusters (YSCs) contribute to the observed UV light of their host galaxies and, via feedback processes, regulate the star formation cycle in the galaxy (A. Adamo et al. 2020, and references therein). While high-resolution studies of star clusters in the Milky Way allow us to dissect single clusters in their stellar, gas, and dust components (e.g., C. Zucker et al. 2023), they suffer from line-of-sight confusion and dust obscuration, which prevent the collection of large, unbiased samples of the cluster population. Probing the entire star cluster population in nearby galaxies is fundamental to understanding star formation as a function of galactic environment and physical properties.

During the last three decades, the Hubble Space Telescope (HST) has paved the way for an unprecedented census of

---

[20] ARC DECRA Fellow.

YSCs in nearby galaxies (B. C. Whitmore et al. 2011; R. Chandar et al. 2014; L. C. Johnson et al. 2016; A. Adamo et al. 2017; M. Messa et al. 2018; J. A. Turner et al. 2022; D. Maschmann et al. 2024, among many others). However, the observed demographics of YSCs, as well as the physical processes behind cluster formation and evolution (e.g., J. M. D. Kruijssen 2015; M. R. Krumholz et al. 2019), cannot be fully understood without grasping the very young stage of life of YSCs, i.e., the emerging phase. In the emerging phase, YSCs are still embedded in their dusty natal cloud and stellar feedback (predominantly photoionization and radiation pressure, K. E. Johnson et al. 2003, 2015; J.-G. Kim et al. 2018; M. R. Krumholz et al. 2019; S. H. Menon et al. 2022; C. Dobbs 2023; D. Pathak et al. 2025) from massive stars dramatically impacts the surroundings, shaping a multi-phase interstellar medium (ISM). This stellar feedback is not instantaneous, and thus, for a certain time, emerging YSCs (eYSCs) are invisible at optical wavelengths and largely missed from the aforementioned optical surveys. M. Messa et al. (2021) estimated that up to 60% of eYSCs are missed for ages between 1 and 5 Myr using near-ultraviolet–optical–near-infrared (NIR) optical HST observations in NGC 1313.

Recently, the advent of JWST has enabled us to detect most, if not all, eYSC populations in nearby galaxies, outside of the Local Group. Thanks to its unprecedented sensitivity and spatial resolution, several campaigns have been characterizing eYSCs and their surrounding star-forming regions in nearby galaxies using JWST NIRCam bands and NIRSpec spectroscopic data (e.g., M. J. Rodríguez et al. 2023; B. C. Whitmore et al. 2023, 2025; R. C. Levy et al. 2024; S. T. Linden et al. 2024; A. Pedrini et al. 2024; J. Sun et al. 2024; A. Knutas et al. 2025). These authors show that eYSCs present an excess of $3.3\,\mu m$ polycyclic aromatic hydrocarbon (PAH) emission from their photo-dissociation regions (PDRs, D. J. Hollenbach & A. G. G. M. Tielens 1999), and they are able to clear their surrounding envelopes due to stellar feedback in a few Myr. However, most of the results presented in these studies rely on correct estimations of eYSC physical properties. Specifically, we need to carefully account for a detailed NIR spectral modeling of emission from star-forming regions in order to obtain accurate derivations of eYSC ages and stellar masses. In optical surveys, single stellar population (SSP) synthesis models that account for stellar and nebular contributions (e.g., yggdrasil E. Zackrisson et al. 2011) have been extensively leveraged and can successfully describe the spectral energy distribution (SED) of YSCs with ages down to ~5 Myr, where the results become extremely sensitive to the most massive stars included in the model, and the way those massive stars form and evolve (A. Wofford et al. 2016). In this respect, due to pre-JWST low sensitivity and resolution of NIR observations in nearby galaxies, models for NIR stellar isochrones have been less explored/tested. Moreover, the NIR is not only sensitive to ionized gas and stellar continuum but also to the complex emission of dust around stars and in PDRs (R. Indebetouw et al. 2006; E. Peeters et al. 2024; R. Chown et al. 2025; I. Schroetter et al. 2024). With JWST, we can now resolve individual extragalactic star clusters, their associated compact H II region, and warm dust in proximity of the newly formed stars within the Local Volume ($d < 11$ Mpc) at parsec-scale resolution.

The Feedback in Emerging Extragalactic Star Clusters (FEAST, GO 1783, PI A.Adamo) survey plays a key role in advancing the observational interpretation of extragalactic eYSC at parsec scales. FEAST encompasses JWST/NIRCam observations of six nearby galaxies spanning a wide range of physical properties. Moreover, these observations were designed to both sample large fields of view (covering most of the targets) and achieve high resolution, allowing for statistical studies of individual eYSCs within single galaxies (B. Gregg et al. 2024; A. Adamo et al. 2025, in preparation). This survey aims to investigate the primary physical mechanisms driving the emergence of eYSCs by measuring levels of obscuration across clusters at different evolutionary stages, and exploring how these trends correlate with the galactic environment. B. Gregg et al. (2024) analyzed the relation between star formation rate and $3.3\,\mu m$ PAH emission for eYSCs in NGC 628, finding that age variations and physical properties of PAHs might have strong impacts on the linearity of this relation. In B. Gregg et al. (2025), the authors have explored variations in this relation as a function of galactic physical properties across the diverse FEAST sample of galaxies. Furthermore, A. Pedrini et al. (2024) illustrated that eYSCs in NGC 628 are linked to star-forming regions where H II regions and PDRs traced by $3.3\,\mu m$ PAH emission are still compact, and their morphology is constrained by cluster evolution. A. Knutas et al. (2025) have studied the eYSC population in M83, with a specific focus on the emerging timescales of eYSCs in different environments within the galaxy disk as well as cluster mass.

With these unprecedented results on the demography of eYSCs in nearby galaxies, comes the need for comprehensive models that accurately describe the SED of eYSCs. In this context, the excellent sensitivity provided by JWST has revealed populations of embedded clusters that present stellar masses ranging from tens to tens of thousands of $M_\odot$ (e.g., A. Knutas et al. 2025, S. T. Linden et al. 2025, in preparation). In this low-mass regime, stochastic effects due to initial mass function (IMF) sampling are no longer negligible, and a full consideration of these effects becomes necessary (J. Maíz Apellániz 2009; D. Calzetti et al. 2010). Under these conditions, distinguishing the main sources of emission from eYSCs in the NIR window becomes crucial for a more complete understanding and interpretation of their NIR SED.

In this paper, we use JWST/NIRCam observations and ancillary HST data to present a multiwavelength analysis of the UV–optical–NIR SED of eYSCs in M51, M83, NGC 628, and NGC 4449, which are part of the FEAST survey. In particular, we derive physical properties of eYSCs using state-of-the-art SED fitting codes and discuss their performances, with a specific focus on the NIR wavelengths. After an introduction of the observations and the eYSC populations (Section 2), we present the adopted SED fitting methodology (Section 3). The results presented in this paper (Section 3.3) reveal discrepancies between the NIR-recovered best fluxes from models and our observations (Section 4). We discuss possible explanations in detail and various interpretations of this issue, focusing on the analysis of the impact of stochastic IMF sampling effects (Section 5). The paper ends with our conclusions and a summary of findings in Section 6.

2. Imaging Data

2.1. Feast Galaxies

For this paper, we use the observations of four galaxies, part of the FEAST program: M51, M83, NGC 628, and NGC 4449.

Table 1
Summary of the FEAST Galaxies Analyzed in this Paper

Galaxy	d (Mpc)	$\log(M_*/M_\odot)$	SFR ($M_\odot$ yr^{-1})	$12 + \log(O/H)$	Foreground A_V	# eYSCI
M51	7.5 (7)	10.38 (1)	6.88 (1)	8.65 (3)	0.095 (9)	1707
M83	4.7 (8)	10.53 (2)	4.17 (2)	8.9 (4)	0.182 (9)	1087
NGC 628	9.84 (6)	10.34 (2)	1.74 (2)	8.51 (3)	0.192 (9)	784
NGC 4449	4.0 (5)	9.04 (1)	0.94 (1)	8.26 (10)	0.053 (9)	249

Note. From left to right: distance, stellar mass, UV extinction corrected star formation rate (SFR), central metallicity from H II regions oxygen abundance, foreground Milky Way attenuation and number of eYSCI presented in this work (see Section 2.2). Reference dictionary: (1) D. Calzetti et al. (2015), (2) A. K. Leroy et al. (2021), (3) D. A. Berg et al. (2020), (4) F. Bresolin et al. (2016), (5) E. Sabbi et al. (2018), (6) R. B. Tully et al. (2009), (7) G. Csörnyei et al. (2023), (8) R. B. Tully et al. (2013), (9) E. F. Schlafly & D. P. Finkbeiner (2011), (10) L. S. Pilyugin et al. (2015).

Table 2
Overview of the Observational Data

Galaxy	JWST/NIRCam	HST
M51	F115W, F150W, F187N, F200W, F300M, F335M, F405N, F444W	WFC3/F275W, WFC3/F336W, ACS/F435W, ACS/F555W, ACS/F658N, WFC3/F689M, ACS/F814W
M83	F115W, F150W, F187N, F200W, F300M, F335M, F405N, F444W	WFC3/F225W, WFC3/F275W, WFC3/F336W, WFC3/F438W, WFC3/F547M, WFC3/F555W, WFC3/F657N, WFC3/F689M, WFC3/F814W
NGC 628	F115W, F150W, F187N, F200W, F277W, F335M, F405N, F444W	WFC3/F275W, WFC3/F336W, ACS/F435W, ACS/F555W, ACS/F658N, ACS/F814W
NGC 4449	F115W, F150W, F187N, F200W, F300M, F335M, F405N, F444W	WFC3/F275W, WFC3/F336W, ACS/F435W, ACS/F555W, ACS/F658N, ACS/F814W

Note. HST/WFC3 observations are from #13340 (Van Dyk), #12762 (Kuntz), #13364 (Calzetti), #17225 (Calzetti), #11360 (O'Connell) and #12513 (Blair). HST/ACS observations are from #10452 (Beckwith), #9796 (Miller), #10402 (Chandar) and #10585 (Aloisi).

The properties of these galaxies are summarized in Table 1. JWST/NIRCam observations of M51, M83, NGC 628, and NGC 4449 have been obtained between 2023 January and 2024 June as part of the FEAST program. For each galaxy, we obtained simultaneous observations in short wavelengths (F115W, F150W, F187N, F200W) and long wavelength channels (F300M, F335M, F405N, F444W). In NGC 628, the F277W filter replaced the F300M. We exploited a FULLBOX 4TIGHT dither pattern to ensure high-quality sampling with large fields of view (e.g., $2' \times 6'$ in NGC 628) and of the point spread functions (PSFs). We refer to A. Adamo et al. (2025, in preparation) for an in-depth description of the data reduction, while here we present an overview of the main steps. Our NIRCam observations have been downloaded from the Mikulski Archive for Space Telescopes (MAST). We reduced the data using the distributed pipeline (version 1.12.5) with calibration data context number 1169.

For these galaxies, we downloaded additional available HST archival observations covering the UV-optical range from the MAST archive, and we reduced them using standard data-reduction steps (see A. Adamo et al. 2025, in preparation). Additional information on these ancillary data is found in Table 2, which presents an overview of the filters employed in this analysis across the sample of galaxies. Finally, we resampled both NIRCam and HST mosaics to a common pixel grid of $0\rlap{.}''04$ pix^{-1} and we aligned them to the same reference system using GAIA (Gaia Collaboration et al. 2023).

2.2. eYSC Catalogs

Stellar feedback mechanisms in eYSCs produce H II regions and PDRs that can be directly traced with multiple JWST/NIRCam filters. In particular, the F187N and F405N filters trace emission from the hydrogen recombination lines Paα and Brα, respectively. On the other hand, the 3.3 μm PAH feature observed by means of the F335M filter represents an optimal tracer for PDRs in star-forming regions (e.g., E. Peeters et al. 2024; R. Chown et al. 2025). For these reasons, we based our selection of eYSCs on their photometric properties in the aforementioned filters. We present and describe the full methodology to detect and classify eYSCs in A. Adamo et al. (2025, in preparation). Here we summarize the main steps. We identified eYSCs as peaked emission in the NIR hydrogen recombination lines (Paα-1.87 μm and Brα-4.05 μm) and in the 3.3 μm PAH feature. As already described in B. Gregg et al. (2024) and A. Pedrini et al. (2024), we refer to this eYSC class as eYSCI, while the eYSCII class represents clusters without compact 3.3 μm PAH emission.

To obtain Paα, Brα, and 3.3 μm PAH maps of our sample of galaxies, we removed the stellar and dust continuum from filters containing the emission features. We subtract the stellar continuum from the F187N filter using the adjacent broad filters F150W and F200W. Since the F200W filter also contains Paα emission, we applied an iterative procedure to remove its contribution, as described in B. Gregg et al. (2024) and D. Calzetti et al. (2024). On the other hand, for the F335M and F405N filters, we removed the stellar and dust continuum using the F300M (F277W in NGC 628) and F444W filters. In the case of F405N, the subtraction was also performed iteratively, as the F444W filter contains Brα emission. This continuum subtraction procedure is fully described in B. Gregg et al. (2024) and results in continuum-subtracted emission line maps for Paα, Brα, and the 3.3 μm PAH feature.

We present now the identification of eYSCI clusters for M51, M83, NGC 628, and NGC 4449. The candidates are independently

identified on the three emission maps using SEP, a Python package for source extraction (K. Barbary 2016), resulting in three different catalogs, one for each emission line map. We then visually inspected all the extracted sources with the aim of recentering and cleaning contaminants in each reference emission map. The catalogs of visually inspected sources are then used to perform aperture photometry in all available JWST and HST sets of filters (see Table 2). For the closer galaxies, M83 and NGC 4449, we adopted an aperture radius of five pixels, which corresponds to physical sizes of ∼4.55 and ∼3.88 pc, respectively. In the case of M51 and NGC 628, we used a radius of four pixels (∼5.8 pc and ∼7.8, a). To correct for background emission, we subtract the mode value estimated from an annulus aperture, centered in the source position, with a radius of seven pixels for both M83 and NGC 4449 and six pixels for M51 and NGC 628. We adopted two pixels for the width of the annulus aperture. Furthermore, we used concentration index-based aperture corrections to account for different point spread functions (PSFs) within the UV-optical-NIR windows (see A. Adamo et al. 2025, in preparation, and A. Knutas et al. 2025).

To obtain the final science-ready catalog of eYSC candidates, we corrected the photometry for Milky Way A_V extinction along the line of sight (Table 1). For each emission map, we produced a photometric catalog containing positions of the eYSC candidates and their flux densities (in mJy and ABmag). To ensure clear detections, we additionally required a magnitude error <0.3 in the F187N and F200W filters for sources extracted from the Paα, and in the F405N (F335M) and F444W filters for sources extracted within the Brα (3.3 μm PAH) map.

As a final step, we matched the three catalogs by their positions to determine their class: eYSCI are detected in Paα and 3.3 μm PAH (Brα, due to the lower resolution, is included but not considered a necessary condition); eYSCIIs are detected in Paα (and possibly Brα); 3.3 μm PAH peak sources do not have a clear peaked emission in Paα and/or Brα. We adopted a four-pixel separation between emission peak centers as our criterion for catalog matching. To test the robustness of this choice, we also performed the matching using five- and six-pixel separations, finding that it introduces only a ∼2% difference in the number of recovered eYSCIs (see also A. Knutas et al. 2025).

For the scientific goal of this paper, we consider only eYSCI with secure detection (signal-to-noise ratio (S/N) > 3) in all eight NIRCam bands. The presence of ionized gas and PAH emission indicates that these objects are young and likely dusty, making this sample ideal for studying cluster SEDs in the NIR wavelengths. This last step leads to the final eYSCI catalogs, which contain 1707, 1087, 784, and 249 objects for M51, M83, NGC 628, and NGC 4449, respectively (last column of Table 1). We present the eYSCI populations in the JWST field of view within the four targets in Figure 1, where the position of each cluster is represented by a black dot. We see a strong association between the eYSCI populations and the spiral structures of M51, NGC 628, M83, and NGC 4449 (although irregular), where we observe enhanced ionized gas emission (Paα, green channel) and PAH emission from the PDRs (red channel) due to intense star formation activity.

2.3. Optical YSC Catalogs

Using HST imaging, we also produced optically identified YSC catalogs for our sample of galaxies. For all the galaxies, the cluster identification is based on compact sources emitting in the HST/F555W filter. In M51, the initial catalog used here relies on the LEGUS (Legacy ExtraGalactic UV Survey, D. Calzetti et al. 2015) catalog presented in M. Messa et al. (2018). Within this catalog, we selected clusters with assigned morphological classes of 1, 2, or 3 (see A. Adamo et al. 2017 for a description of these classes). Moreover, we required these clusters to lie within the JWST field of view, obtaining a final catalog consisting of 2361 YSCs. We adopted a similar procedure for the NGC 4449 LEGUS catalog (B. C. Whitmore et al. 2020), obtaining 573 optically identified YSCs. For M83, we used the optical YSC catalog presented in A. Knutas et al. (2025) and we applied analogous masks and selections as in M51 and NGC 4449, resulting in 3121 cluster candidates. We applied the same method for the optical YSC population in NGC 628 (presented in A. Adamo et al. 2025, in preparation), obtaining 3784 optical YSCs. We note that, on average across the four galaxies, 4% of the optically selected YSCs coincide with the position of an eYSC.

The positions of the cluster candidates (centered using HST/F555W) are used to perform aperture photometry in all the HST and JWST available filters. Aperture photometry, local sky background, and aperture correction are performed by matching the same physical scales in all HST and JWST filters using the same settings as described for the eYSC catalogs in Section 2.2. We will discuss the results obtained with these catalogs, applying the appropriate S/N and age selections, in Section 5.

3. Cigale Modeling

To analyze the 0.2 to 5 μm SEDs of the observed YSCs and eYSCs and to constrain their physical properties (e.g., age, mass, attenuation), we performed SED fitting using the Code Investigating Galaxy Emission (CIGALE; M. Boquien et al. 2019). Although this code is originally designed to fit the SED of galaxies, it has been effectively exploited in the study of star cluster light (J. Fensch et al. 2019; J. A. Turner et al. 2021; A. Pedrini et al. 2024). S. T. Linden et al. (2025, in preparation) presents a detailed complementary analysis showing a performance comparison between CIGALE and an alternative model widely used in cluster analysis (yggdrasil, E. Zackrisson et al. 2011) in recovering physical properties of YSCs and eYSCs in the spiral galaxy NGC 628.

3.1. CIGALE Grid for EYSCs

CIGALE works in two main steps. The first step consists of computing a grid of models that encompasses the generation of stellar, nebular, and dust emission models covering a predefined parameter space. Subsequently, in the second step the code performs a Bayesian-like χ^2 analysis to fit the model grid to the observed cluster SEDs (G. Yang et al. 2020). As a result, CIGALE outputs the best values for the input-defined parameter space, as well as best-fit fluxes for each filter. For each galaxy, we used the final eYSCI catalogs as input observation files. For the HST filters, we flagged the observed flux in a given filter as an upper limit if the S/N ratio is lower than 3.
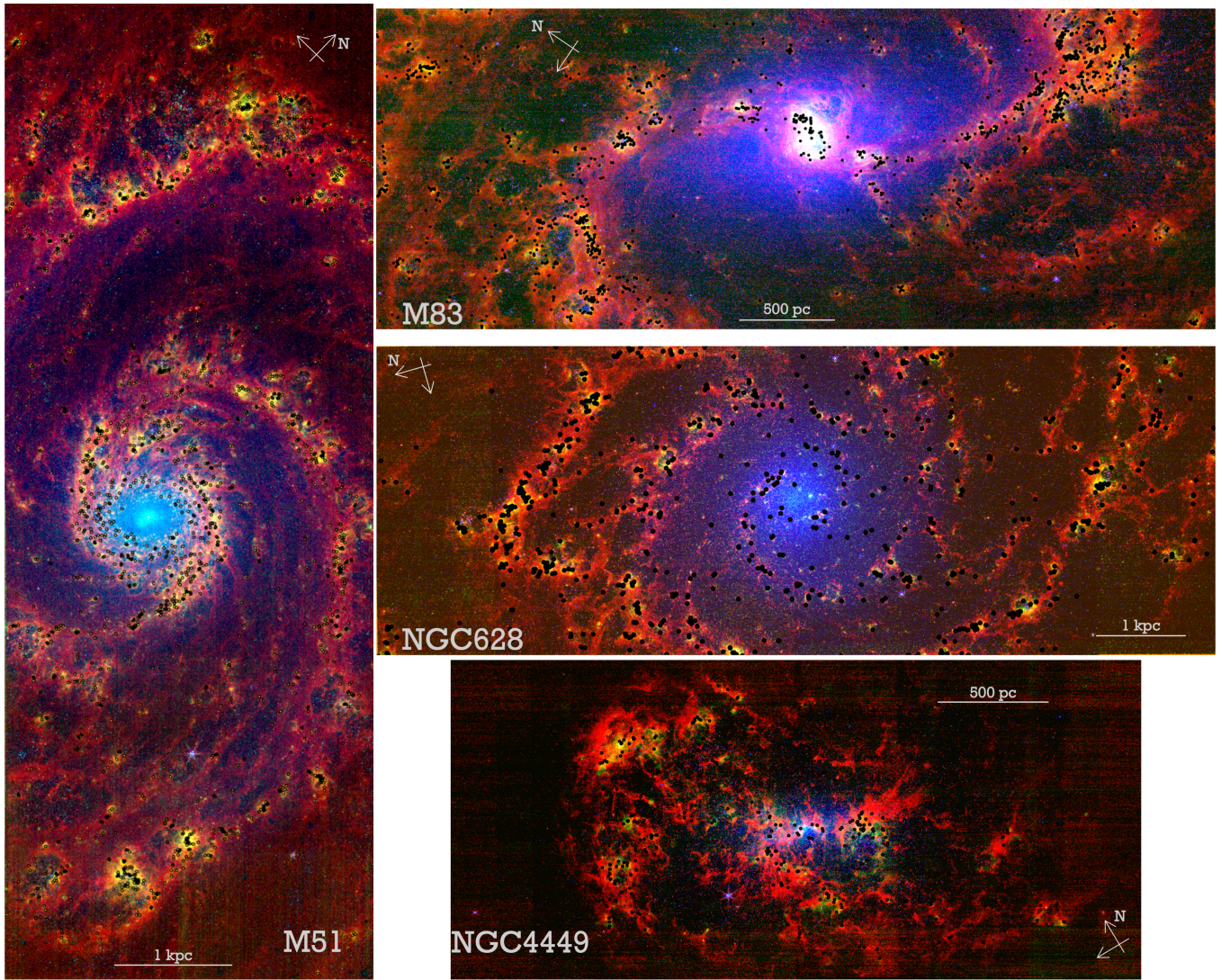
Figure 1. NIRCam detected eYSC populations in M51 (left panel), M83 (top right panel), NGC 628 (middle right panel), and NGC 4449 (bottom right panel). For each galaxy, the RGB color scheme is the following: F335M continuum subtracted map (red), F187N continuum subtracted map (green), F115W map (blue). For NGC 628, we replaced F187N with F405N due to the better visual quality of the map. We highlight the position of the eYSC populations with black dots. In the three spiral galaxies, eYSCs are located along the spiral arms, where they are associated with the highest concentration of star-forming regions in the galactic disks.

As input for the CIGALE models, we use the parameter grid designed in S. T. Linden et al. (2025, in preparation), shown in Table 3. We consider an eYSC SED to be generated by an instantaneous burst of star formation, which consists of a decaying exponential function of timescale 0.001 Myr. As clusters are identified as bright sources in Paα, we limit the age range of the stellar population to vary between 1 and 10 Myr with steps of 1 Myr. The stellar emission is modeled from the G. Bruzual & S. Charlot (2003) stellar models, considering a G. Chabrier (2003) IMF and solar metallicity (40% solar for NGC 4449). Nebular emission models are based on CLOUDY grids (A. K. Inoue 2011; G. J. Ferland et al. 2013; M. Boquien et al. 2019). To account for dust attenuation, we use the modified starburst model, which allows the user to parameterize the starburst attenuation law from D. Calzetti et al. (2000). Additionally, the `E_BV_factor` parameter (Table 3) regulates the reduction factor between the attenuation computed for the emission lines and the stellar continuum attenuation. For the emission lines, we adopted a Milky Way extinction curve (see M. Boquien et al. 2019 for details in the attenuation model). Finally, we use the dust emission templates from B. T. Draine et al. (2014).

3.1.1. Testing Parameter Choice in Cigale

CIGALE uses several parameters to control the dust and ionized gas emission, as introduced in the previous section and presented in Table 3. In general, we observe that changing the parameter grid for nebular gas emission ($\log(U)$, n_e, f_{esc}, f_{dust}) does not change the recovered physical parameters or the goodness of the fit (χ^2) in a noticeable way. However, the inclusion of the nebular continuum and emission in the models is fundamental to fit the fluxes in the narrow bands centered on Hα, Paα, and Brα. In Appendix A, we show the impact of including/excluding the narrowband filters from the SED of the optical YSCs in NGC 4449. As already shown by B. C. Whitmore et al. (2020), the inclusion of at least one narrowband transmitting a hydrogen emission line (e.g., Hα) mitigates the age-extinction degeneracy. We compare the 0.2–to–5 μm FEAST SED outputs, including narrowbands, with

Table 3
CIGALE Adopted Grid, as Described in Section 3

Parameter	Type	Values
tau_main*	SFH	0.001 Myr
age	SFH	1–10 Myr (step 1 Myr)
tau_burst*	SFH	0.001 Myr
burst_age*	SFH	1 Myr
f_burst*	SFH	0
sfr_0*	SFH	1.0
normalize*	SFH	True
imf	Stellar	G. Chabrier (2003)
metallicity*	Stellar	0.02 (0.008 for NGC 4449)
separation_age*	Stellar	10 Myr
logU	Nebular	−3.5, −3.0, −2.5, −2.0
zgas*	Nebular	0.02 (0.008 for NGC 4449)
ne	Nebular	10, 100 cm^{-3}
f_esc	Nebular	0.01, 0.1, 0.2, 0.3, 0.4, 0.5, 0.6
f_dust	Nebular	0.01, 0.1, 0.2, 0.3
lines_width*	Nebular	50 km s^{-1}
E_BV_lines	Attenuation	0.01, 0.1 to 5.0 (step 0.1)
E_BV_factor	Attenuation	0.4, 0.5, 0.6, 0.8, 1.0
uv_bump_wavelength*	Attenuation	217.5 nm
uv_bump_width*	Attenuation	35.0 nm
uv_bump_amplitude*	Attenuation	0.0 nm
Ext_law_emission_lines	Attenuation	Milky Way (J. A. Cardelli et al. 1989)
Rv*	Attenuation	3.1
qpah	Dust	0.47, 1.12, 1.77, 2.50, 3.19, 3.90, 4.58
umin	Dust	0.3, 0.5, 0.7, 1.0 *informed grid: 1,10*
alpha*	Dust	2.0
gamma	Dust	0.01, 0.05, 0.1, 0.5 *informed grid: 0.5,1*

Note. Fixed parameters are marked with *.

the previous output of B. C. Whitmore et al. (2020), showing a very good agreement with the analysis performed by previous teams. We conclude that as long as at least one nebular line is included in the cluster SED fit, then the results are relatively insensitive to the nebular grid choice.

As for the dust parameters, we noticed a significant impact on the resulting recovered cluster physical properties. Taken at face value, we do not have enough information in our SEDs to derive stringent constraints on the dust. The dust parameters require observational constraints in the mid-infrared–far-infrared (MIR-FIR) wavelength range, which falls outside our observations and cannot be obtained at the physical scales studied here. Parameters linked to dust heating and dust mass heated in star-forming regions, such as U_{min} and γ (umin and gamma in Table 3), correlate with dust emission at 24 μm, 71 μm, and 160 μm (B. T. Draine & A. Li 2007). Similarly, 60–100 μm observations can constrain the power law coefficient α (D. A. Dale et al. 2014, alpha in Table 3). Observations of MIR-FIR integrated light from local galaxies have showed that U_{min} ranges between 1 and 10, while γ yields best-fit values of 0.5–1 (B. T. Draine et al. 2007) and α is generally fixed to 2 (B. T. Draine & A. Li 2007). Based on these findings we fitted the SEDs using an informed (IF) grid, where we constrain U_{min} to be either 1 or 10, while the allowed

values for γ are 0.5 and 1, following B. T. Draine et al. (2007). We do not impose any additional constraints on the possible values of q_{PAH}, as this quantity depends on the incident radiation field and local ISM conditions (e.g., J. Chastenet et al. 2019). By inspecting the recovered dust parameter distributions (see Figure 2 for M51), we noticed different results compared to the parameter grid of Table 3. For this reason, we have explored a larger grid and investigated the favored parameter space when fitting. We refer to the model grid that provides the best fit as the adopted (AD) grid shown in Table 3, with less strict constraints on U_{min} and γ compared to the IF one.

Since our observations are limited to the NIR spectrum, we can evaluate the effect of these parameters only on the quality of the CIGALE fits to the optical and NIR SEDs. In Figure 2 we present a comparison between CIGALE results for eYSCI in M51 obtained with the AD grid and with an IF grid, where the only difference is the constraints on U_{min} and γ (Table 3).

This figure shows that the recovered reduced χ^2 is lower for eYSCI fitted with the AD grid. Additionally, when looking at the fitted age distribution, a large fraction of eYSCI fitted with the IF grid settles at the edge of the parameter space, returning either young ages or old ones. Moreover, as a side check, we note that our results for the AD grid remain consistent even when we additionally include $U_{min} = 10$ and $\gamma = 1$.

Hence, we conclude that our AD grid gives better results in terms of the quality of the fits. We must stress that since we cannot constrain the dust parameters, there is no physical reason associated with the choice of the dust grid behind this consideration (see Section 5.2 for a further discussion). However, this unexpected behavior calls for a careful analysis of the eYSC SEDs, trying to unveil the reason behind this result (see also S. T. Linden et al. (2025, in preparation) for a more detailed exploration of eYSCs in NGC 628).

3.2. CIGALE Grid for Optical Catalogs

Due to the different nature of optically selected YSCs (see Section 2.3), the CIGALE adopted grid for these specific objects requires small modifications from the eYSCs grid presented in Table 3. Since these clusters are identified in the V band, there are no prior constraints on their age, and therefore, we allow the age parameter vary from 1 Myr to 14 Gyr. Additionally, optically selected clusters present a lower value of $E(B - V)$ (e.g., B. C. Whitmore et al. 2020, A. Knutas et al. 2025). For this reason, we limit the E_BV_lines parameter grid to 1.5. In the specific case of NGC 4449, the metallicity grid was extended to include 0.004 in addition to 0.008. For the optical YSC catalog in NGC 4449, Appendix A presents a comparison between the ages we derived using CIGALE in this work and those recovered by B. C. Whitmore et al. (2020) from the LEGUS survey for the same objects, showing good agreement when filters that include hydrogen emission lines are used in the fit.

3.3. Fitting Results

In this section, we present an overview of the results obtained with CIGALE for eYSCI in our sample of galaxies. Final photometric catalogs and CIGALE SED fit outputs will be released at https://feast-survey.github.io. We listed the number of eYSCIs for each galaxy in Table 1.

Figure 3 illustrates the results of the best recovered values for age, stellar mass, and attenuation $E(B - V)$. Histograms are
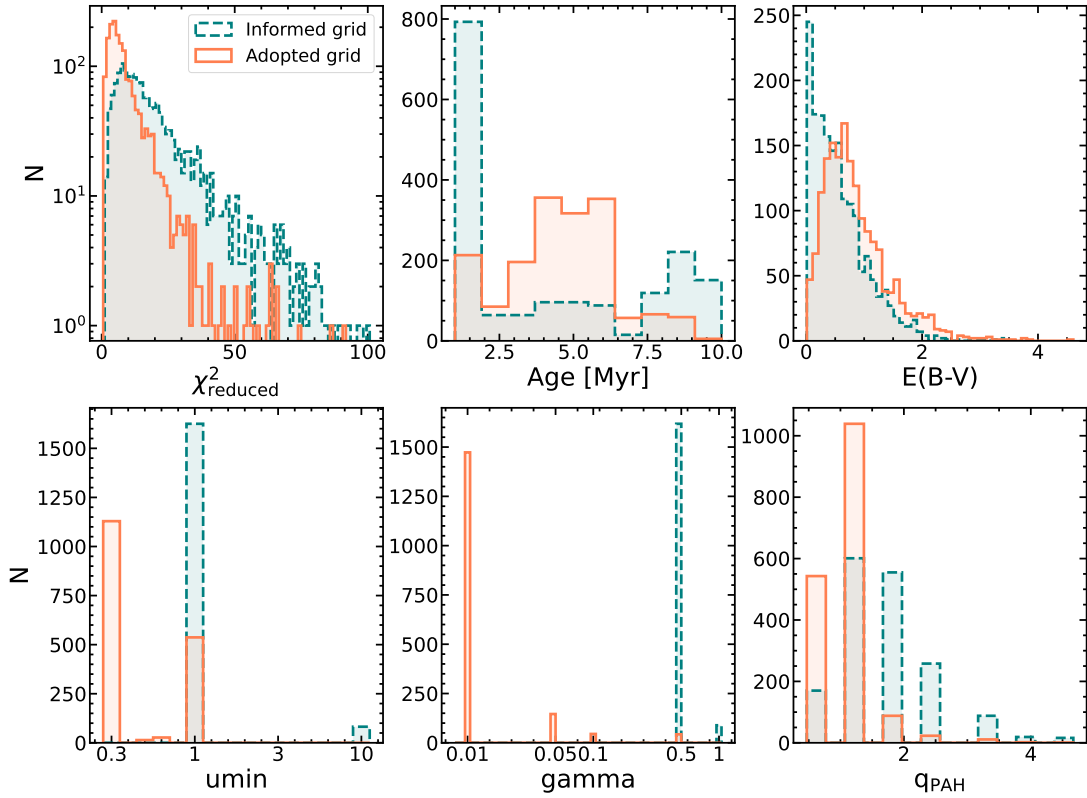
Figure 2. Recovered $\chi^2_{\mathrm{reduced}}$, Age, $E(B - V)$, U_{min}, γ and q_{PAH} distributions from CIGALE for two different grids in M51. While the orange histograms show the results for the grid adopted in this paper (see Table 3), the blue distributions result from the empirically motivated dust grid (IF grid), as described in the text.
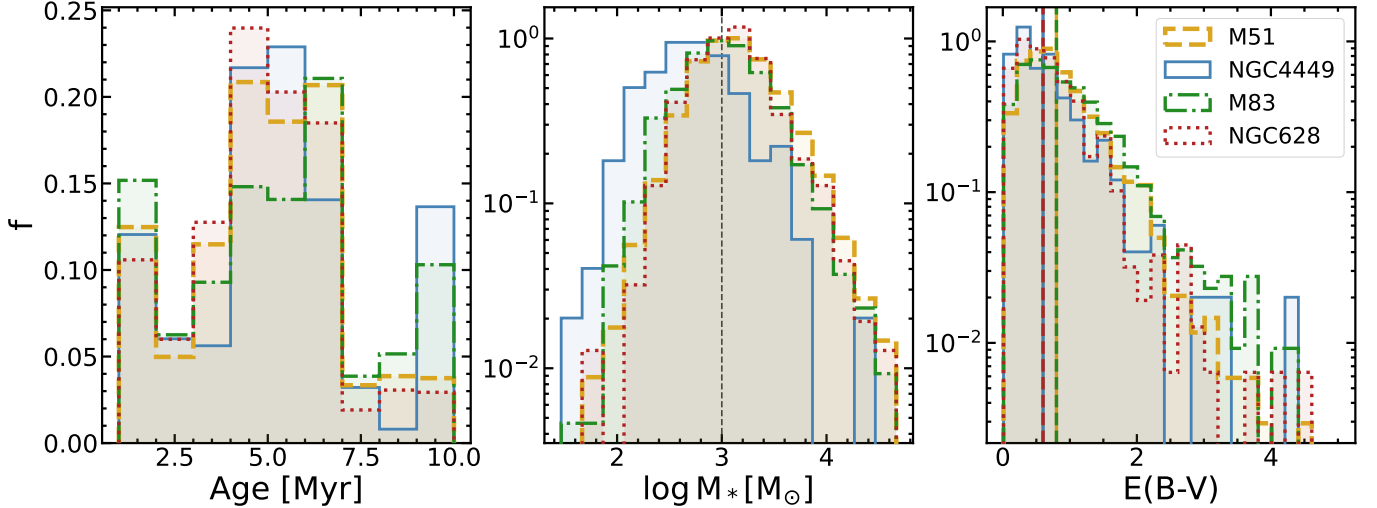

Figure 3. Normalized distributions of age, stellar mass, and $E(B - V)$ for eYSCs in our sample of galaxies, obtained with CIGALE. We use different colors and line styles to distinguish the distributions of each galaxy. In the middle panel, we drew a dashed line at $M_* = 1000\, M_\odot$ to guide the plot visualization. In the right panel, we added median values of the $E(B - V)$ distributions as vertical lines.

color-coded by different galaxies. These plots show that eYSCs in our sample of galaxies share similar behavior in the distributions. The age distributions exhibit a steep drop after 6 Myr due to the fact that older clusters produce a considerable smaller fraction of ionizing photons than the younger counterpart (C. Leitherer et al. 1999; D. Calzetti 2013). The mass distributions show similar trends as each other. NGC 4449 presents overall lower masses. We observe a similar scenario in the $E(B - V)$ distributions. In this case, M51 and M83 show higher $E(B - V)$, with median values of

about 0.8 mag., while NGC 628 and NGC 4449 show slightly lower values with medians of 0.6 mag for both distributions, consistent with what found by B. Gregg et al. (2024, 2025) for these galaxies using the Hα/Paα ratio.

To better understand the meaning of these results, we visually inspected a set of representative SEDs from the CIGALE output, where models are compared with observations. In Figure 4 we present four representative examples of eYSCI SEDs in M51. In this figure, the observed fluxes in each filter (blue unfilled squares) are compared to the corresponding best flux values
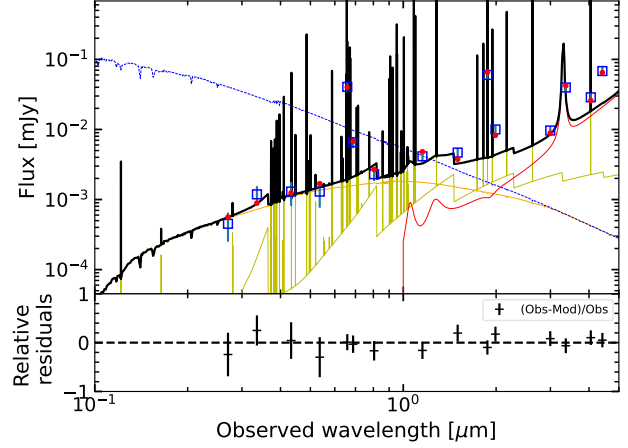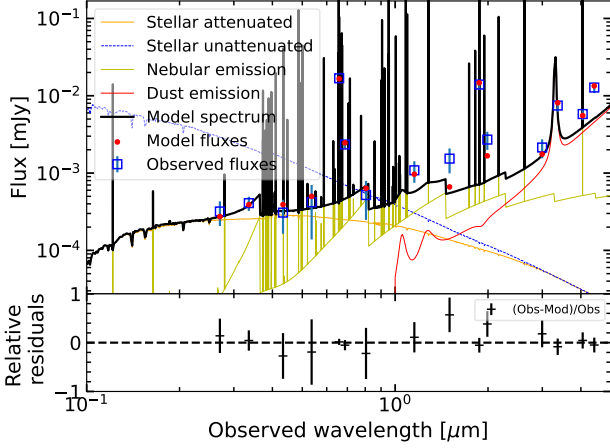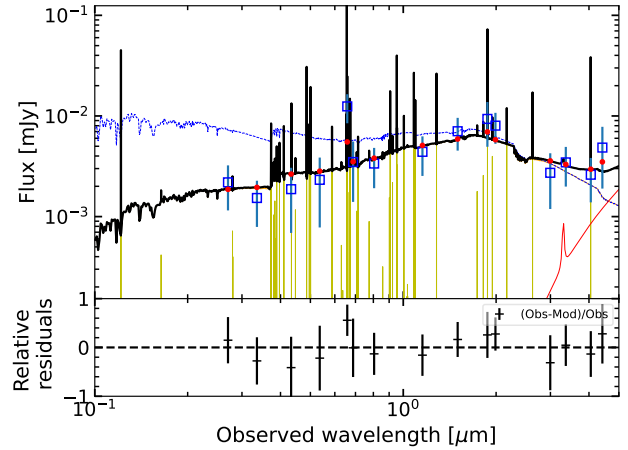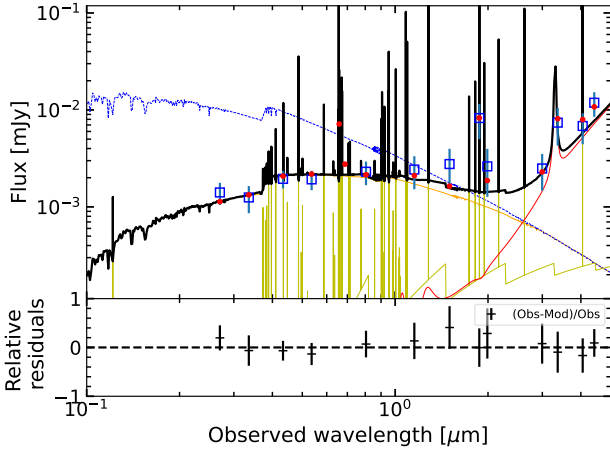
Figure 4. Observed SEDs, best-fit models and recovered best fluxes for four representative eYSCs in M51. For each panel, the title of the plot describes the fitted properties of the specific eYSC (represented by a unique ID): $\chi^2_{\mathrm{reduced}}$, age, and stellar mass. The observed fluxes in HST and JWST filters are shown with blue squares with error bars, while we show the CIGALE best-fitted fluxes convolved to each filter throughput with red filled circles. The black line represents the best model spectrum, while the remaining colored lines correspond to best-fitted models for the attenuated and unattenuated stellar component (orange and blue spectra, respectively), nebular (green spectrum), and dust emission (red spectrum). For each filter, we show the relative residual fluxes (obs − best)/obs in the lower portion of the panel.

recovered by CIGALE (red filled circles). Underneath those points, we show the best model grid returned by the code. We show the residuals of the fit in the bottom panel as (obs − best)/obs, where obs is the observed flux and best is the best-fitted value, for each filter. The title of each plot describes the fitted properties of the given eYSCI in term of id, best reduced χ^2 value, best age and best stellar mass.

Already from these representative cases, we note that regardless of the reduced χ^2 values, the CIGALE modeling is not able to fully reproduce the SED of the clusters. We find that the quality of the fit depends on the recovered age and mass of the eYSC. In the top left panel, we present the best-fitted model for an eYSC with a fitted age of 1 Myr and M_* of 361.16 $M_\odot$. Even though the recovered χ^2_{red} suggests a good quality of the fit, it becomes evident that some NIR broad bands appear underestimated in the CIGALE fit. In this case, the observed fluxes are systematically higher than the best-fit values, even when accounting for the uncertainties. This issue is particularly evident for the F150W filter and the offset between the best-fit values and the observations seems to decrease in amplitude (or even disappear) going toward either

higher masses (top right panel of Figure 4) or older ages (bottom panels of Figure 4). This discrepancy is what we will refer in the next section as the NIR excess.

4. NIR Excess

The CIGALE modeling presented in the previous section reveals the presence of an observed NIR flux excess that the best-fit models cannot recover. In this section, we further quantify this excess over the entire sample of eYSCI.

We calculate the residual difference between the magnitude returned by CIGALE, m_{CIG}, and the observed magnitude, m_{obs}. For this analysis we limit ourselves to eYSCI that are well detected in all the NIRCam bands (see Section 2.2). If a specific HST-UV/optical magnitude is included in the residual analysis, we require that the eYSCI have been detected with an S/N > 3 in that filter.

We use the M51 cluster population as a reference, but we apply the same analysis to all FEAST galaxies introduced above. In Figure 5, we plot the distributions of the residuals, i.e., the difference $m_{\mathrm{CIG}} - m_{\mathrm{obs}}$ for the following filters: HST/ F555W, F814W and JWST-NIRCam/F115W, F150W,
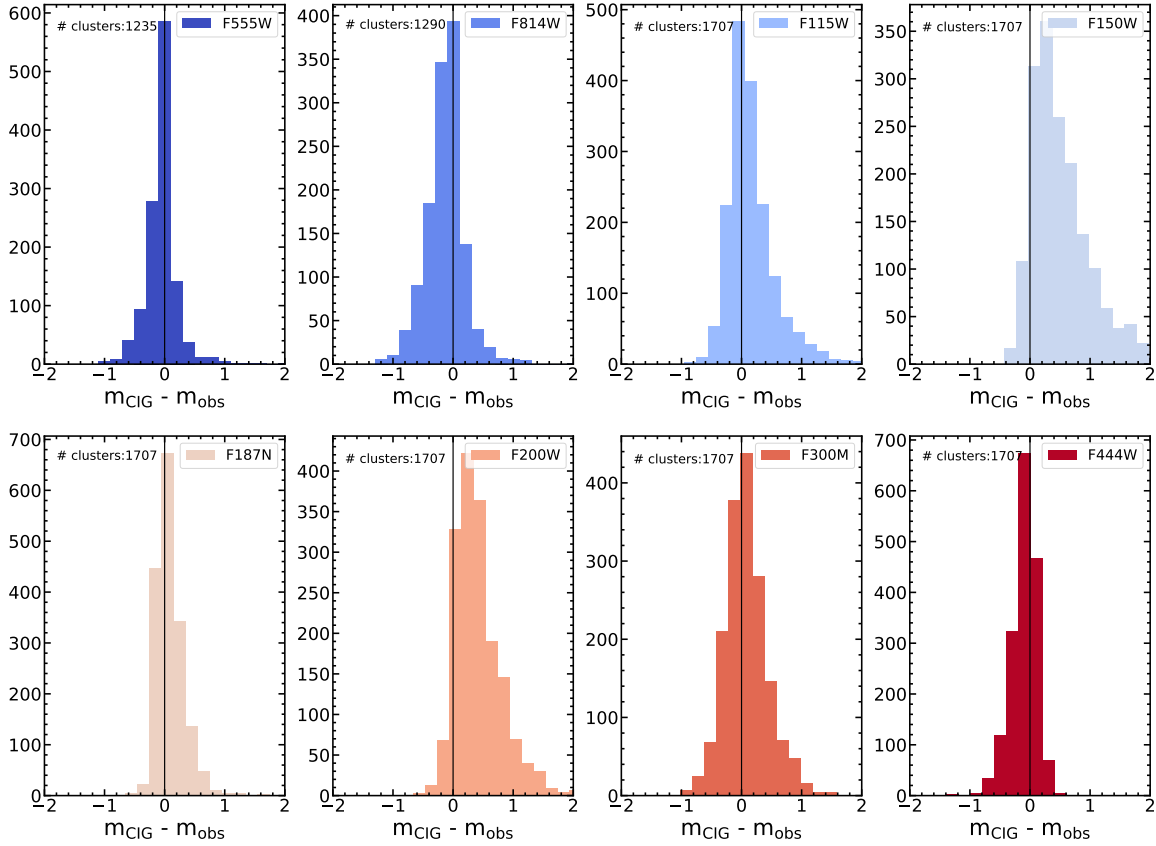
Figure 5. Distributions of the residuals $m_{CIG} - m_{obs}$ in eight selected filters (F555W, F814W, F115W, F150W, F187N, F200W, F300M, F444W) for the sample of eYSCI in M51. For each filter, $m_{CIG} - m_{obs}$ represents the difference in magnitude between the best-fitted flux from the CIGALE fit and the observed flux, respectively. For each panel, we show the total number of eYSCI, which varies in HST filters due to the additional S/N requirements described in the text. To guide the reader's eye, we plot a black vertical line at $m_{CIG} - m_{obs} = 0$.

F187N, F200W, F300M, and F444W. We note that the number of eYSCIs in the HST bands is lower than the number in the four NIRCam bands due to the S/N requirement we applied for the single HST bands. For each filter, a distribution centered on $\Delta m \simeq 0$ would indicate a good agreement between models computed by CIGALE and observations. On the other hand, a prominent tail in the distributions at $\Delta m > 0$ would indicate that the observed flux in that filter is brighter than the one predicted by the best-fitted model, i.e., the latter model underestimates the recovered flux.

The Δm distributions in Figure 5 show some interesting trends. In general, we see that the fluxes in the HST/F555W, NIRCam/F187N, F300M, F444W, are centered around zero (see the relative numbers of objects in the peak ($\Delta m \pm 0.2$ mag) with respect to the wings). On the other hand, the distributions in NIRCam/F150W and F200W indeed show a prominent tail going toward positive values of Δm, meaning that the best-fitted models cannot properly reproduce the observed fluxes in a large fraction of systems. The HST/F814W residuals appear to suffer from the opposite behavior, i.e., the best solution that attempts to fit the NIR excess would underperform in the bluer band. These widespread trends, along with the "unconstrained" grid of dust parameters discussed above, suggest an underlying severe problem for CIGALE to reproduce the observed SEDs of the eYSCs.

To better investigate this result, we unfold the residuals in each available filter of each galaxy by using the recovered ages and masses of the eYSCs. We present the median values and 16th–84th percentiles of the Δm in Figure 6. We divide our

samples of eYSCI into three age bins (1–3 Myr in purple, 3–6 Myr in blue, 6–10 Myr in orange) and two mass bins ($M_* \leqslant 3000 \, M_\odot$ as squares and $M_* > 3000 \, M_\odot$ as triangles). The three age bins represent three different evolutionary stages of eYSCI, while the two mass bins roughly distinguish between cluster that possibly fully sample the IMF (higher-mass bin) and clusters that might be subjected to stochastic sampling effects (M. Cerviño & V. Luridiana 2004). In general, all the sub-samples defined in this analysis are statistically significant, with the number of eYSCIs in each bin ranging from tens to hundreds. For the three spirals, ~80% of the eYSCI have fitted masses $\leqslant 3000 \, M_\odot$, and 40 % have masses below ~1000 $M_\odot$. In the case of NGC 4449, we omitted the high mass bin, as this galaxy shows only 16 eYSCI with fitted mass higher than 3000 $M_\odot$. As a guidance, we also include the median values of the whole sample as black crosses.

The medians of the full populations (black crosses), as already demonstrated in Figure 5, show an observed NIR excess in the broad-band filters F150W and F200W of all the targets, and in F277W of NGC 628 (the only galaxy for which this filter is available at the time of this work). The F300M, which replaced the F277W, does not seem to be significantly affected. As we look at the residuals per cluster age and mass bins, some interesting trends are evident. Clusters fitted with ages younger than 6 Myr and masses less than 3000 $M_\odot$ (purple and blue filled squares) appear to be the ones driving most of the recovered positive residuals in the F150W and F200W (and F277W). In particular, the excess is highest in
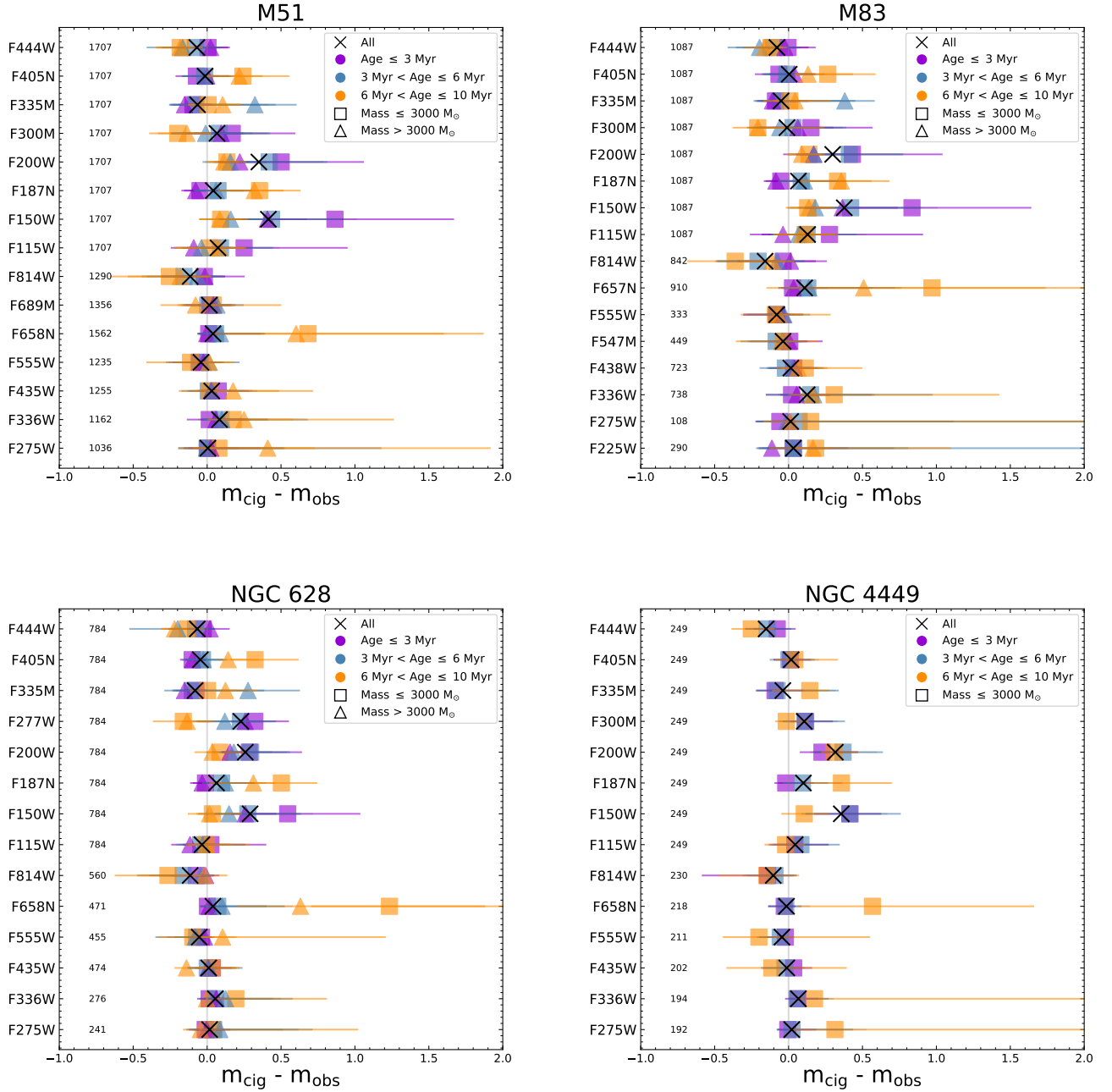
Figure 6. Median values of the residual distributions $m_{CIG} - m_{obs}$ (see Figure 5) for each available filter in eYSCI across the four galaxies studied in this work. For each panel, black crosses represent the corresponding median value of $m_{CIG} - m_{obs}$ in that specific filter, for the entire population of eYSCI (where the total number of clusters is specified in the plot for each filter). HST filters present smaller numbers of clusters due to the additional S/N criteria we applied in this analysis. Different colors represent sub-samples of the population of eYSCI binned by the best-fitted age recovered with CIGALE. Additionally, we use two different symbols (square and triangle) to distinguish between two bins of masses ($\leqslant 3000\ M_\odot$, $> 3000\ M_\odot$). For each data point, error bars correspond to the 16th–84th percentile of the residual distribution. Every galaxy in our sample exhibits an excess in the NIR, particularly more offset can be seen for the low mass and young ($\leqslant 3$ Myr) bins.

F150W for the low mass clusters younger than 3 Myr (purple square). In all galaxies, the eYSCI fitted with ages older than 6 Myr (orange symbols) are the ones with the largest residuals in all the narrow bands. Particularly telling for this group is the inability of CIGALE to provide a best-fit model that reproduces the excess in the narrowband filters transmitting Hα (HST/F657N and F658N), Paα (NRCam/F187N), Brα (NIRCam/F405N). We conclude that the recovered physical properties for this ("older") group are not correct, and due to the presence of strong ionized hydrogen line emissions, these clusters are likely younger. We additionally checked for trends between the observed NIR excess in the F150W filter and the

attenuation $E(B - V)$ of the clusters, finding no significant correlation between them (Pearson correlation test: $r = -0.075$, $p = 0.002$).

Another important consideration to make is that while we observe similar trends in all groups and average populations of all the galaxies of the sample, the amplitude of this model-observed difference appears to vary as a function of the host galaxy. In particular, the magnitude in the NIR excess in the young and low mass bin in NGC 4449 is lower than the one observed in the spiral galaxies, and among the spirals, the residuals in the eYSCI population of NGC 628 are slightly smaller.

5. Discussion

The recovered NIR excess presented in the previous section brings more uncertainties and makes the interpretation of the physical parameters derived with CIGALE (e.g., Figure 3) more challenging. As noticed in the previous section, the inability of the models to reproduce the observed eYSC SEDs results in errors in the recovered cluster ages (up to a factor of ~2, due to the presence of hydrogen emission lines) and may lead to incorrect conclusions about star formation timescales. Here we first test whether the parameter choice to perform photometry might be at the root of the problem, and we discuss/test other, more physical reasons.

5.1. The Effect of Extraction Aperture on the Recovered Cluster SEDs

It is well known in the literature that the use of large apertures when studying star clusters leads to severe contamination, especially in the NIR bands (N. Bastian et al. 2014). As star cluster sizes range on average between 2 and 4 pc (M. R. Krumholz et al. 2019), using apertures of the order of 5–10 times the cluster size results in a flux excess from contaminants which are not necessarily associated with the cluster emission. This effect appears to be stronger in the NIR wavelengths where red super giant stars can contaminate the photometry (N. Bastian et al. 2014).

The apertures in our study, however, are much smaller and provide cluster photometry at a physical scale of 3–6 pc and, therefore, we are confident the photometry presented in this work does not present significant contamination from external sources. Nonetheless, we further verified the aperture effect and tested apertures of four, five, and six pixels to check whether the excess strongly increases for larger apertures. In Appendix B, we show the representative results of this analysis in M83, one of the closest galaxies in our sample with a high number of detected eYSCs. We select the smallest radius to be four pixels, since this aperture size is still larger or comparable to the full width at half maximum of the reddest filter F444W (~3.6 pixels, J. Rigby et al. 2023). This test confirms that the excess residuals get stronger for apertures of six pixels (~5.5 pc). For the closer galaxies (M83 and NGC 4449), using either four or five pixels does not imply a significant change, while for the more distant ones (NGC 628 and M51), the excess residual gets stronger at five pixels. For these reasons, we adopted photometric radii of four pixels for the more distant galaxies in our sample, while we used five pixels for the closest ones. In conclusion, increasing the aperture results in a more pronounced NIR excess, as already pointed out in the literature, but the excess is still significant when small apertures are adopted.

5.2. Testing Dust Models on the SED Fit Analyses

Another source of uncertainty might come from the inability of our data to inform CIGALE on the dust properties. While JWST offers MIR coverage up to 20 μm, the reduced spatial resolution implies an increase in the size of the adopted photometric aperture, and therefore an increase in the NIR excess and contamination discussed in the previous Section. As already described in Section 3.1.1, the resulting dust parameter grid we use is the one that gives the lowest values of χ^2 in the CIGALE outputs, but the ranges are quite off from what we would have expected from MIR-FIR constraints (e.g.,
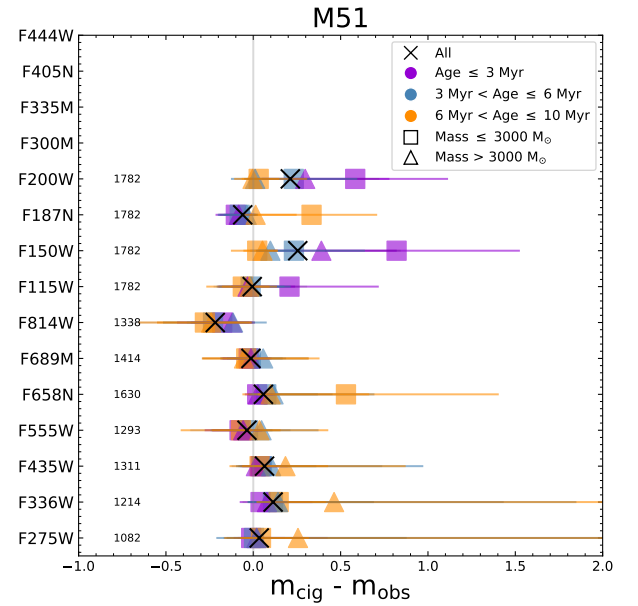

Figure 7. Median values of the residual distributions $m_{CIG} - m_{obs}$ for eYSCI in M51, as shown in the top left panel of Figure 6. In this case, the CIGALE SED fit is performed up to the F200W filter and ignoring the contribution from the dust models.

U_{min} and γ, see Section 3.1.1). It is perhaps likely that this behavior in the models is also driven by the presence of the NIR excess: CIGALE "prefers" unrealistic dust models in the attempt to compensate for a signal that cannot be fitted only with standard SSP models and nebular emission. This might be expected when a model is missing one or more components (e.g., M. L. Peck 1980). To inspect this possibility, we performed a new SED fitting analysis for the eYSCI population in M51, this time with the exclusion of the dust grid from the CIGALE parameter space. Moreover, in the reasonable approximation that PAH and dust emission start to dominate the spectra of star clusters after 2–3 μm, we fitted the eYSCI up to the NIRCam F200W filter. With this method, our SED best-fit values are exclusively constrained by stellar and nebular emission at wavelengths below ~2 μm.

In Figure 7, we show the residual analysis in M51 for this new SED fitting approach. We note that the number of eYSCIs recovered in the NIRCam filters is slightly higher than the complete fit. This is due to the fact that we are considering a smaller number of NIRCam filters when applying the S/N cut defined in Section 2.2. The NIR excess is still evident and exhibits similar trends discussed in Figure 6, regardless of whether dust models are included in the fitting procedure. This result excludes the unconstrained choice of the dust parameter grid as a driver for the observed NIR excess.

5.3. The NIR Excess in Optical YSCs

Taken at face value, the change in the strength of the excess discussed in Section 4 might suggest a relation with age. We therefore investigate the residuals in the optically selected YSC population with fitted age younger than 10 Myr in M51 (with the entire parameter grid and set of filters). As described in Section 2.3, YSCs are identified as bright sources of emission in optical bands. Since they are more evolved and less dusty, we expect them to show a limited contribution from emission in the NIR. Clusters where their SED is dominated by
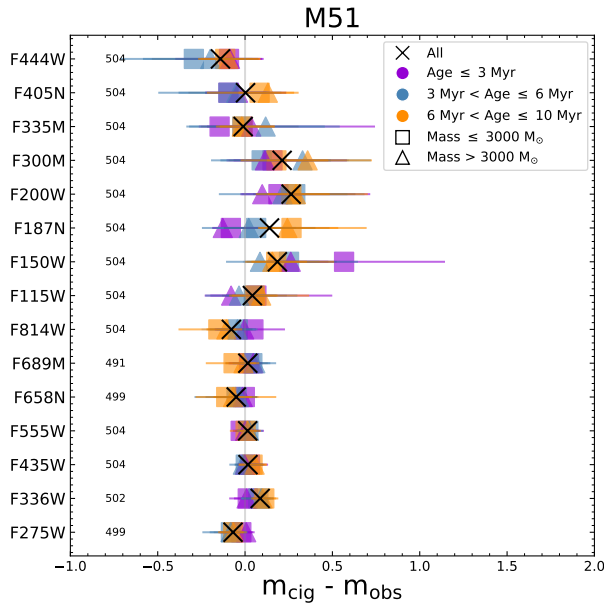
Figure 8. Median values of the residual distributions $m_{CIG} - m_{obs}$ for the optically selected YSC population in M51 younger than 10 Myr. The layout of the figure is as presented in Figure 6.

stellar and nebular emission are ideal for understanding how dust models are influencing the results. For the scope of this analysis, and to avoid adding further uncertainties, we select only YSCs detected in all NIRCam bands with $S/N > 3$, analogous to what was presented for the eYSCs. We also remind the reader that to be classified as YSCs (see Section 2.3), they must be detected in at least four HST bands as well.

We present the results of the residual analysis for this population in Figure 8. It is evident that the NIR excess is less pronounced in optically selected YSCs in M51, with median residuals going from about 0.5 to 0.2 mag. Moreover, we see that differently from the eYSCI (see Section 4), the hydrogen recombination lines are well fitted. In Appendix C, we confirm these results also for the other three galaxies in the sample.

5.4. The Impact of Stochastically Sampling the IMF

The discrepancy between models and observations observed in this work is not uniform across clusters. As shown in Figure 6, clusters in bins characterized by younger ages and lower masses are more likely to show an NIR excess, while more massive clusters show smaller residuals overall. One of the possible reasons behind this behavior may be linked to IMF sampling issues. For stellar masses below $10^4 \ M_\odot$ (M. Cerviño & V. Luridiana 2004), stochasticity in the IMF sampling becomes important, and it cannot be ignored at masses of a few hundreds of $M_\odot$ (D. Calzetti et al. 2010). For cluster mass ranges where stochasticity becomes important, the number of massive stars, dominating the integrated light and therefore the derived ages and masses, might vary strongly from cluster to cluster with the same mass. For instance, clusters with total stellar masses ranging from a few hundred $M_\odot$ to 1000 $M_\odot$ contain between a few and a few tens of massive stars ($M > 8 \ M_\odot$), respectively (see Figure 1 in E. R. Stanway & J. J. Eldridge 2023). Furthermore, while the optical wavelengths are typically dominated by the massive star's SED, the NIR emission also has an important

contribution from pre-main-sequence (PMS) stars. PMS stars are in an evolutionary stage where the star is still contracting toward the main sequence, making them bright sources in the 1–$2.5 \ \mu$m NIR wavelengths (M. H. Heyer et al. 1990; S. J. Kenyon & L. Hartmann 1995; C. Eiroa et al. 2001). In stellar clusters where stochastic effects are non-negligible (stellar masses $\lesssim 10^4 \ M_\odot$), the variation in the number of massive stars can significantly impact the integrated NIR light. In such cases, the emission from PMS stars may contribute substantially to the observed NIR flux. However, CIGALE employs a deterministic approach in which the IMF is fully sampled, normalized to 1 $M_\odot$, and then rescaled to reproduce the observed SED (M. Boquien et al. 2019). Moreover, stellar spectra models from G. Bruzual & S. Charlot (2003) do not account for PMS stars, which means CIGALE cannot take into account their contribution.

Investigating the impact of a stochastic approach on estimating the NIR colors of eYSCs requires a SED model that includes stochastic sampling of the IMF of star clusters. To reach this goal, we generated star cluster libraries using the stellar population synthesis code `slug` (Stochastically Light Up Galaxies, R. L. da Silva et al. 2012). Given a fixed IMF and a set of parameters that regulate stellar and nebular contributions, `slug` simulates the spectrum and the photometry of a single star cluster, where its stellar population is stochastically sampled from a probability distribution function. For star clusters, `slug` simulates a single burst of star formation with mass either fixed or drawn from a cluster mass function. Consequently, the code follows the evolution of the cluster during time and computes stellar and nebular emission (M. R. Krumholz et al. 2015). We note that `slug` does not include dust models, but allows us to test the NIR colors where we see the excess.

For a fixed star cluster mass and for each age bin, the output of the simulation consists of photometric data from a given set of filters, in ABmag. In terms of this paper's scope, we run 10^4 star cluster models for a set of five fixed values of mass: 500 $M_\odot$, 1000 $M_\odot$, 3000 $M_\odot$, 5000 $M_\odot$, and 10,000 $M_\odot$. The choice of parameters we adopted for `slug` simulations is based on maintaining the highest possible level of consistency with the grid adopted in the CIGALE analysis. For each model, the simulation starts at 1 Myr and ends at 10 Myr, with a time step of 1 Myr. We used a G. Chabrier (2003) IMF, where the minimum mass for the stochastic treatment is set at 0.08 $M_\odot$. Stellar tracks, including emission from PMS stars and rotation, are from A. Dotter (2016), and models for computing stellar atmospheres are based on starburst99 (C. Leitherer et al. 1999). Furthermore, `slug` uses CLOUDY-based templates (G. J. Ferland et al. 2013) to account for nebular emission. We fixed the ionization parameter $\log U$ (see Table 3) to -2.5 and the fraction of ionized photons contributing to nebular emission, ϕ, to 0.73. We do not apply any extinction correction to the output photometry, as this quantity varies across different clusters.

We focus on the NIR bands and we plot the photometry of the simulated `slug` cluster libraries for solar metallicity in Figure 9 (the equivalent figure for 40% solar metallicity models is included in Appendix D). While in the left panel we show the color–color distribution from the NIR broad band filters that show the excess discussed in Section 4, in the right panel we added the narrowband filter F187N and the tracer of Paα emission and therefore of cluster ages to better compare
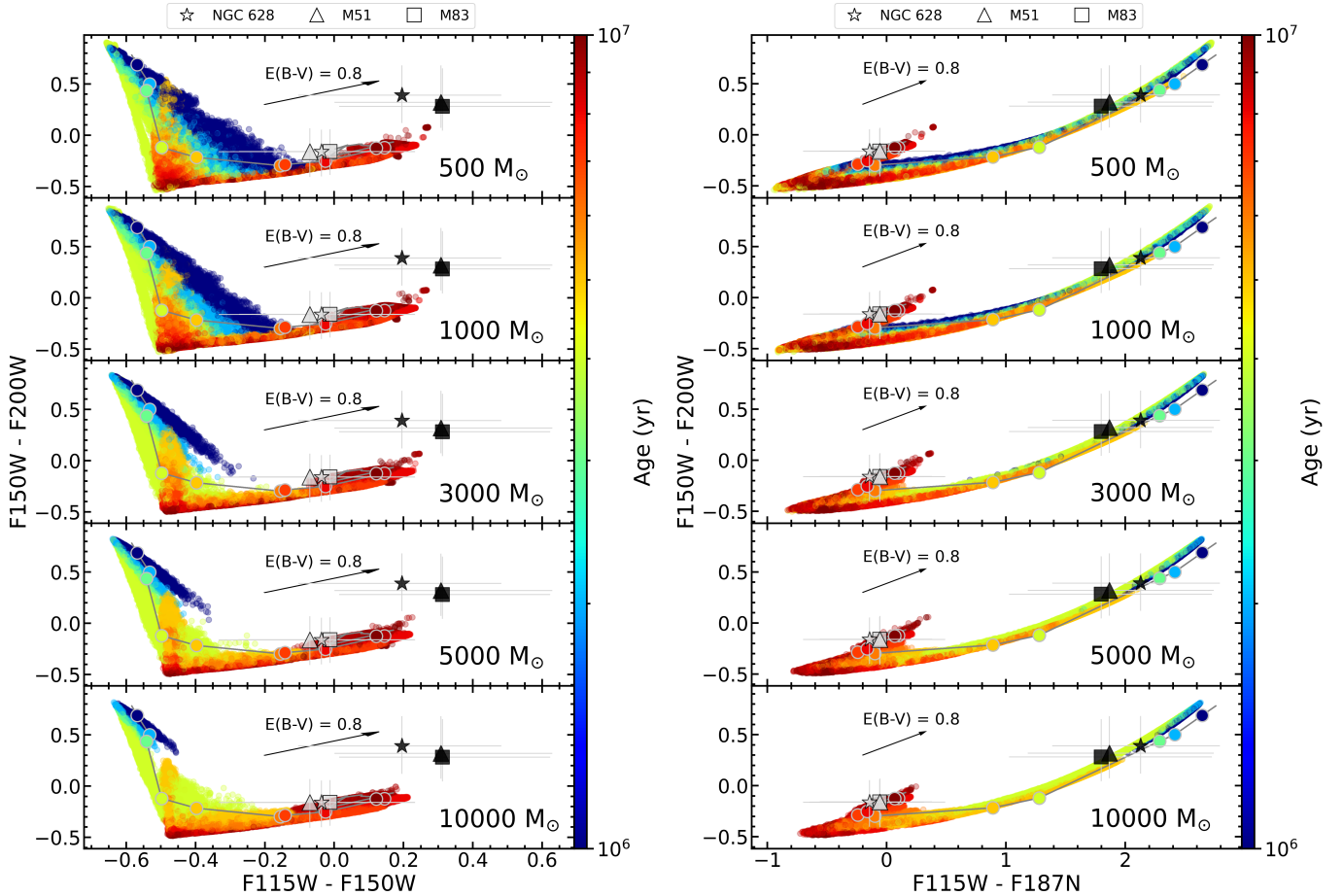
Figure 9. NIR color–color diagrams in ABmag for simulated `slug` cluster libraries with different fixed stellar mass and color-coded by cluster age. The gray line represents a stellar evolutionary track computed with the `yggdrasil` code. Each point of the track is color-coded by age as the `slug` cluster libraries. For an observational comparison, we plotted median values and 16th–84th percentiles for the young cluster population in M51, NGC 628 and M83. We show the eYSCI populations with black symbols, while gray symbols represent the optically identified YSC populations younger than 10 Myr and with a fitted $E(B-V) < 0.1$, for a better comparison with the dust-free libraries. The extinction law vectors are from K. Fahrion & G. De Marchi (2023).

our observations with the models. In this plot, for a specific value of mass, the simulated libraries of star clusters are represented by filled circles color-coded by age. In addition, we plot an evolutionary track from the `yggdrasil` code (gray line), where each bin of age is color-coded as the cluster library. The track is modeled for a 1000 $M_\odot$ cluster with solar metallicity, $f_{cov} = 0.5$ and $E(B-V) = 0$. Similar to CIGALE, the `yggdrasil` tracks are computed using a deterministic approach and are shown here for comparison against the `slug` libraries. Finally, we report median values of observed colors in M51, NGC 628, and M83 (for NGC 4449, see Appendix D) for eYSCI (black symbols) and optical identified clusters younger than 10 Myr and with fitted $E(B-V) < 0.1$ (gray symbols; see Section 2.3).

In the left panel of Figure 9, we note that modeling emission from clusters using a stochastic approach can strongly impact the color differences of the NIR bands for low mass and young clusters. Focusing on a specific bin of younger ages (<5–6 Myr), the recovered scatter in the NIR color–color distributions significantly increases going toward lower mass bins. For instance, at 1 Myr (blue circles), the scatter F115W − F150W in the x-axis goes from ∼0.5 mag at 500 $M_\odot$ to ∼0.1 mag at 10,000 $M_\odot$. This effect also manifests as a scatter around the `yggdrasil` tracks. For older clusters (7–10 Myr, orange to red circles), the spread becomes less

evident as the NIR bands start being dominated by the presence of more evolved stars. In the right panels of Figure 9, the inclusion of the narrowband filter transmitting Paα scatters the color F115W − F187N over more than 2 mag at very young ages, especially for low mass clusters (<). We conclude that the recovered physical properties for1000 $M_\odot$). Even in this color–color space the direction of reddening, stochastic sampling, and age coincide.

The median values recovered from observations in the four galaxies confirm that optically selected YSCs are, on average, older than eYSCs, with the median values settling where simulated clusters indicate ages from 6 to 10 Myr. We therefore expect that PMS stars have little contribution to their NIR colors.

On the other hand, eYSCs are, on average, younger, and their NIR colors might be partially explained by models that include both stochastic effects and attenuation as primary factors. The median value for fitted values of $E(B-V)$ we presented in Section 3.3 indicates a reddening for eYSCs that is consistent with the reddening vector plotted in the figure, suggesting that both attenuation and stochastic sampling would move the models closer to the median colors of the eYSCs. The right panel of Figure 9 indicates that the median ages of these sources in these galaxies are, at face value, close to 4–5 Myr old. However, the correction for extinction would

make them younger than the median values obtained with CIGALE.

This analysis efficiently demonstrated that a stochastic approach, as well as the inclusion of PMS stars in the SED modeling process, might be important in understanding the NIR emission coming from low mass eYSCs. For instance, in the age range from 1 to 3 Myr and for stellar masses of 500–1000 $M_\odot$, the average scatter between `slug` and the `yggdrasil` track in the F115W − F150W color is approximately 0.35 mag. The scatter observed in Figure 6 for the low mass bin and the same range of ages is about 0.6 mag for the spiral galaxies and about 0.4 for NGC 4449. While the NIR excess observed for NGC 4449 makes stochastic IMF sampling combined with extinction a more likely explanation, for the spiral (metal-rich) environments, it suggests that this effect alone might not be sufficient to explain the observed discrepancy. We will further discuss the observed differences between spirals and NGC 4449 in the next section.

An additional caveat to consider when quantifying the observed NIR excess using `slug` concerns the modeling of PMS stars within SSP synthesis codes. For low-mass stars, the choice of the initial stellar radius sets the internal entropy content, which in turn determines the stellar properties during the first ∼5 Myr (T. Hosokawa et al. 2011; L. Haemmerlé et al. 2019). Furthermore, observations have revealed that PMS stars undergo a dynamic accretion history, leading to a spread in entropy at birth (T. R. Hunter et al. 2017; S. S. Jensen & T. Haugbølle 2018). For low-mass stars with low effective temperatures, this effect can be significant and may help explain why stochastic models still fail to fully reproduce the observed NIR scatter.

5.5. Missing Ingredients to Reproduce the 1–to–5 μm SED of eYSC

Stellar evolutionary models included in `slug` account for PMS stars, but do not include emission from hot dust coming from their inner circumstellar disk and/or envelope surrounding accreting stellar cores. The spectra of a very young star (young stellar object (YSO), e.g., R. A. Gutermuth et al. 2011) surrounded by a dusty disk (proto-planetary disk, e.g., C. J. Lada 1987), present prominent emissions in NIR wavelengths that have been addressed as "NIR excess" (L. A. Hillenbrand et al. 1998), displaying redder colors when compared to only stellar emission. YSO SEDs will also contribute to the 3–to–5 μm. Thus, their inclusion might also alleviate the unrealistic dust grid models that the fit is currently preferring as presented in Section 3.

In general, strong radiation fields may contribute to the dissolution of dusty disks; various studies have shown that proto-planetary disks can survive in regions of high and embedded star formation (e.g., A. J. W. Richert et al. 2015, 2018). Moreover, in a recent review, A. J. Winter & T. J. Haworth (2022) illustrated that disks in low mass star-forming regions are, on average, more likely to survive than their higher mass counterparts. The fact that the observed infrared excess is strongest for the lower-mass eYSCI could indicate that the contribution of YSOs might be an ingredient to consider in interpreting the SEDs of star clusters. This could be further tested with the inclusion of these additional models in SED fitting codes.

Furthermore, we noted above that the recovered residuals in NGC 4449 are smaller. Various studies have shown that in low

metallicity environments proto-planetary disks might have less shielding from dust and therefore go toward a faster photo-evaporation (e.g., C. Yasui et al. 2010; R. Matsukoba et al. 2024). On the other hand, G. De Marchi et al. (2024) investigated this issue using JWST NIRSpec observations of a sample of candidates accreting PMS stars. The authors concluded that PMS stars in lower metallicity environments ($1/8\ Z_\odot$) efficiently maintain proto-planetary disks longer than solar metallicity counterparts, challenging the previous interpretation.

While a contribution from YSOs may be crucial to explain the NIR excess observed in this work, a combination of additional phenomena must also be considered for a comprehensive understanding.

For example, we note that our SED fitting methodology does not account for the clumpiness of the dust distribution. Nonisotropic dust geometries can have a non-negligible impact on the NIR SEDs of clusters and on the resulting mass estimates (e.g., R. Indebetouw et al. 2006; D. G. Whelan et al. 2011).

Binary interactions and rotation-driven processes can also inject NIR light into the SED of a YSC. For instance, classical Be stars are fast rotators surrounded by a dust-free gaseous disk that emits significantly in the NIR (A. Meilland et al. 2012). In addition, Wolf–Rayet stars, which are the classical examples of hydrogen-stripped cores, are known to exhibit NIR excesses, as characterized by several previous IR surveys (e.g., K. E. Johnson et al. 2004; P. A. Crowther et al. 2006; J. C. Mauerhan et al. 2009, 2011).

Finally, we note that our results rely on the assumption that each object in our sample is a single star cluster formed during a single burst of star formation (see Section 3) and can therefore be described by an SSP model. In reality, we acknowledge that some clusters may instead consist of multiple sub-clusters, potentially leading to an age spread of a few Myr.

5.6. Impact on Physical Properties

We investigated how the observed discrepancy between models and NIR observations affects the age estimates of eYSCs. To this end, we independently rederived cluster ages using Paα equivalent width (EW) measurements.

We estimated Paα EWs using our photometric data as

$$EW_{Pa\alpha} = \frac{F_{\lambda,line}}{F_{\lambda,cont}} BW_{F187N}, \qquad (1)$$

with $F_{\lambda,line} = F_{\lambda,tot} - F_{\lambda,cont}$ being the intrinsic flux density of the Paα emission line, $F_{\lambda,tot}$ the total flux density measured in the F187N filter and $F_{\lambda,cont}$ the measured underlying continuum resulting from the interpolation of a blue component (F150W) and a red one (F200W), using the same reasoning for continuum subtraction presented in Section 2.2. BW_{F187N} corresponds to the nominal bandwidth of the F187N filter: 240 Å.[21] We did not apply any extinction as the Paα EW is only marginally affected by it (M. Messa et al. 2021). To estimate eYSCI ages we interpolated the Paα EWs obtained from our samples of eYSCI in M51, M83, NGC 628, and NGC 4449, with recovered EWs from the `yggdrasil` tracks

---

[21] https://jwst-docs.stsci.edu/jwst-near-infrared-camera/nircam-instrumentation/nircam-filters#gsc.tab=0
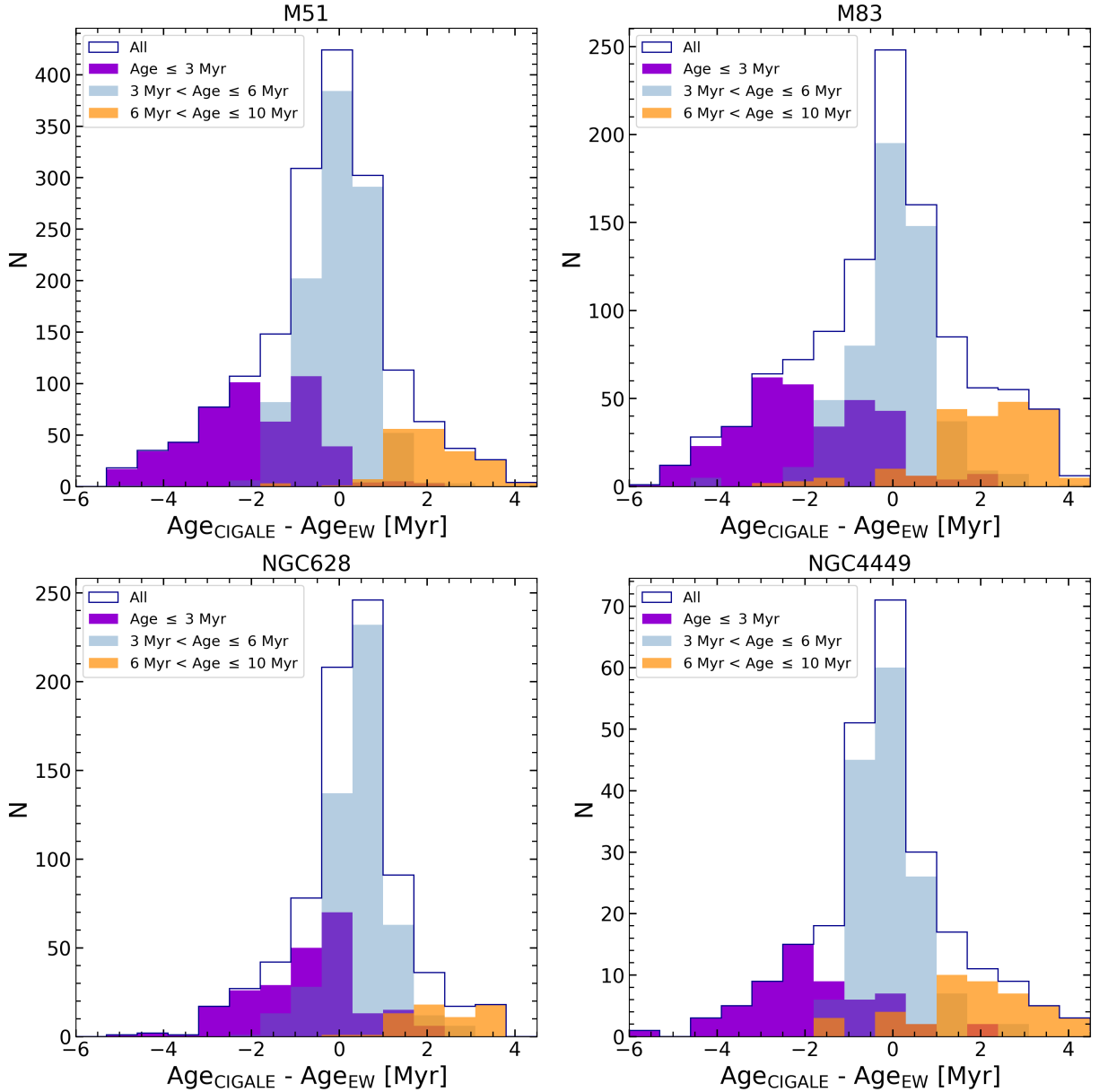
Figure 10. Distribution of age differences for eYSCI in M51, M83, NGC 628, and NGC 4449, obtained using two different methods. For each panel, on the *x*-axis, Age_{CIGALE} represents the best-fit values of age from CIGALE, while Age_{EW} is estimated from Paα EWs, as described in Section 5.6. The unfilled histogram shows the entire population of eYSCI in the four FEAST galaxies, while we use filled histograms to compare the age differences using as a reference the CIGALE bin of ages defined in Section 4. Age bins are color-coded as in Figure 6.

introduced in Section 5.4. In the case of NGC 4449, we used a stellar track with 40% solar metallicity.

We compare the recovered eYSCI ages from CIGALE and the EW method in Figure 10. The blue unfilled distribution shows the age difference for the entire eYSCI populations in the four FEAST galaxies, while filled histograms correspond to the distributions binned by the CIGALE best-fitted ages (see Section 4) and color-coded as in Figure 6.

Overall, we find that age differences between the CIGALE and EW methods are, on average, within ∼1 Myr in 80% of the cluster population analyzed in this work. However, we also recovered larger deviations. The subsample of eYSCs with ages older than 6 Myr in the CIGALE fit (orange colors in Figure 6) shows EWs consistent with significantly younger ages, in agreement with the fact that they are still associated with

considerable ionized H emission. The subset of eYSCI with CIGALE best ages <3 Myr (purple) shows older EW ages. These trends may result from different underlying causes.

It is reasonable to assume that the EW estimates might be affected by the NIR excess in the continuum underlying Paα. CIGALE and other evolutionary models like yggdrasil do not account for additional components in the NIR, and consequently, the interpolated observed EWs might be underestimated, biasing the age distribution toward older values. This effect could be major in a regime where the contribution to the observed flux from the source of the excess is higher than the continuum produced by the stellar population models. Based on the measured excess in the <3 Myr subsample (purple distributions), this impact is not negligible for ∼30%–40% of the objects, potentially leading to lower EWs and thus older inferred ages.
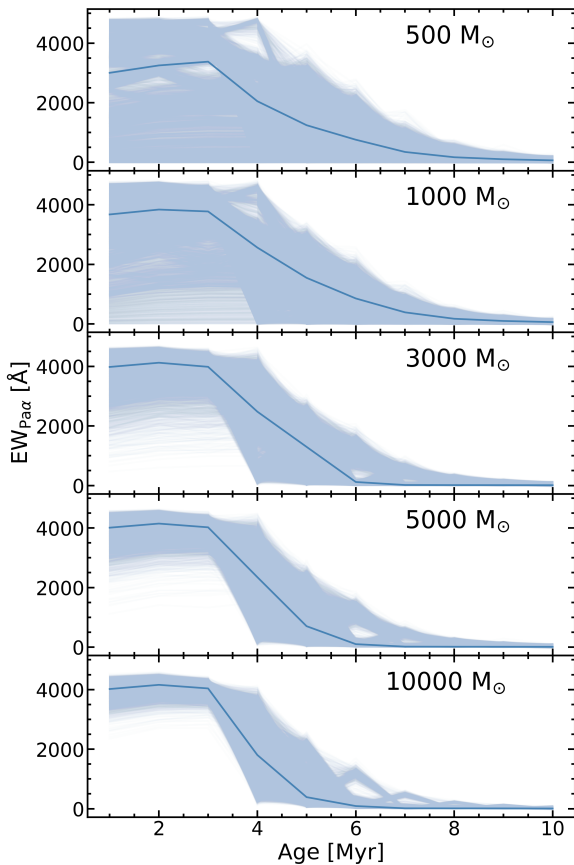
Figure 11. Paα EW as a function of age for simulated `slug` cluster libraries with different fixed stellar masses of 500, 1000, 3000, 5000, and 10,000 $M_\odot$, as defined in Section 5.4. Each panel corresponds to a specific stellar mass, as indicated by the label. The darker lines represent the median tracks of the simulated populations.

Finally, stochastic IMF sampling also affects the EW–age relation commonly used in the literature. In Figure 11, we present the recovered Paα EWs from our `slug` simulations (see Section 5.4) as a function of age for different cluster masses. For each mass bin, the darker lines indicate the median values. We find significant differences across cluster masses, both in individual realizations and in the median trends. In the low mass bins, the EW–age relation breaks down: for example, a low observed EW could correspond to either a young or an old cluster. The relation only emerges for cluster masses larger than 5000 $M_\odot$. These trends imply that even EW measurements cannot be trusted as age indicators.

Our analysis suggests that caution must be taken when interpreting results that rely on inferred physical properties of eYSCs.

6. Conclusions

In this paper, we used HST and JWST/NIRCam observations to analyze the SEDs of the population of eYSCI in four galaxies from the FEAST survey: M51, M83, NGC 628, and NGC 4449. These clusters are selected to be well detected in ionized hydrogen emission (Paα) and to exhibit a prominent 3.3 μm PAH feature from their surrounding PDRs, indicating that they are very young (<10 Myr) and possibly dusty. After thoroughly exploring the fitting parameter space (see Section 3), we modeled their SEDs using the CIGALE fitting

code. The main findings of this analysis are summarized as follows:

1. The dust parameter grid that yields better fits with CIGALE deviates from expectations based on MIR-FIR studies of star-forming regions. The adopted dust grid in this work is not physically motivated, but rather chosen solely based on the quality of the fits.

2. We identify an NIR flux excess that cannot be fully reproduced by current models. We find that the CIGALE fits in the F150W and F200W filters reveal a systematic discrepancy, with the best-fit fluxes underestimating the observed values. We investigated whether observational biases or the choice of model parameters could resolve this discrepancy and conclude that they cannot account for the observed excess. This excess may originate from one or more stellar or hot dust components in the SED that are not accounted for in existing models.

3. The observed NIR excess correlates with the ages and stellar masses of the eYSCs. Young (age ⩽ 3 Myr) and low-mass ($M_\star \leqslant 3000\ M_\odot$) clusters exhibit the strongest positive residuals of about 0.3–0.6 mag in F150W and F200W. Clusters with fitted ages >6 Myr do not show a prominent broadband excess; however, high residuals in the narrowbands F187N and F405N, tracing ionized gas, suggest that these sources may in fact be younger than inferred from the best fit.

4. We explored the effects of stochastic IMF sampling using the `slug` code. Our results show that both stochasticity and the inclusion of PMS stellar emission in the models might partially account for the observed color excess and consequently the unconstrained dust grids. We further speculate that including emission from YSOs may be essential to reduce these discrepancies.

5. We investigated the impact of the observed NIR excess on age estimates. We derive the cluster ages using color–color distributions, SED fits and EW estimates. These different methods point toward very YSC populations; however, none of them yield reliable absolute age determinations.

Our results highlight the limitations of current SED fitting tools like CIGALE in modeling eYSC SEDs, particularly in reproducing the observed NIR properties. The NIR excess is most pronounced in very young (⩽3 Myr), low-mass systems. In these regimes, stochastic effects, PMS star evolution, YSO disk emission, and other additional contributions discussed in the text may become increasingly important, yTet are not fully captured in standard models. Ideally, future tools would incorporate stochastic sampling across all stellar evolutionary phases and include more realistic treatments of both stellar and dust emission in young clusters. To minimize systematics due to modeling assumptions, such tools would benefit from a design in which different components of the models can be turned on or off, allowing for a more controlled exploration of their individual effects on the resulting SEDs.

Appendix A
Comparison of SED Fitting with Exclusion of H Emission Lines

This section of the appendix presents a comparison between our age estimates for optically selected YSCs in NGC 4449 obtained with CIGALE, as described in the main text, and previous results from the LEGUS survey (D. Calzetti et al. 2015). The goal of this test is to highlight the importance of including hydrogen recombination lines in the SED fitting of YSCs. In the left panel of Figure 12, we compare our age estimates with those derived using only HST broadbands (F275W, F336W, F435W, F555W, F814W; B. C. Whitmore et al. 2020). In the right panel, by contrast, the LEGUS ages are derived with the addition of the $H\alpha$ emission line (F658N; B. C. Whitmore et al. 2020). As this comparison shows, the inclusion of even a single hydrogen recombination line in the SED significantly improves the fit quality, helping to mitigate the age-extinction degeneracy.
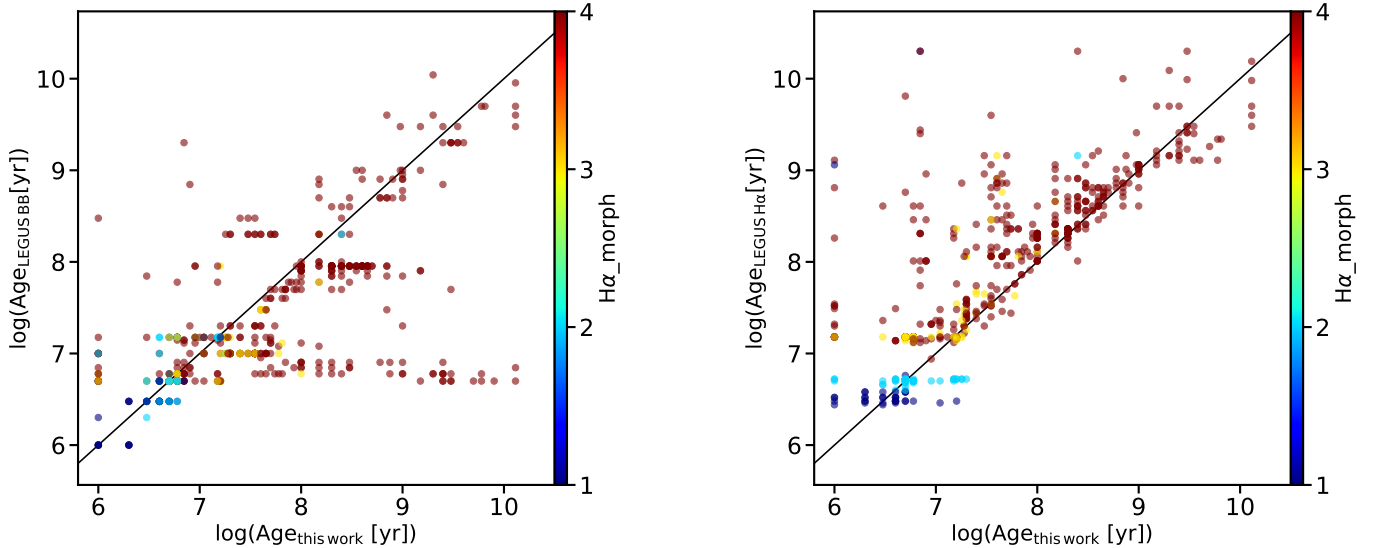

Figure 12. Comparison between the CIGALE-estimated ages of the optical YSC population in NGC 4449 (see Section 2.3) and the age estimates from the LEGUS survey (B. C. Whitmore et al. 2020). In the left panel, LEGUS ages are derived using only broadband filters, while in the right panel, the $H\alpha$ recombination line is included. The color bar indicates the $H\alpha$ morphology (from 1: strong $H\alpha$ emission, to 4: no $H\alpha$), as described in B. C. Whitmore et al. (2020).

Appendix B
Aperture Effects in M83

As introduced in Section 5, we tested different photometric aperture sizes to assess the impact on the observed NIR excess. Here, we present this analysis for one of the FEAST targets: M83. While the photometric radius adopted in the main analysis is 5 pixels, Figure 13 shows the corresponding residual analysis for apertures of 4 pixels (left panel) and 6 pixels (right panel), analogous to the one shown in the top right panel of Figure 6. As discussed in the text, we do not observe significant changes in the NIR excess when using apertures of 4 or 5 pixels. However, the residuals increase when a 6 pixel aperture is used.
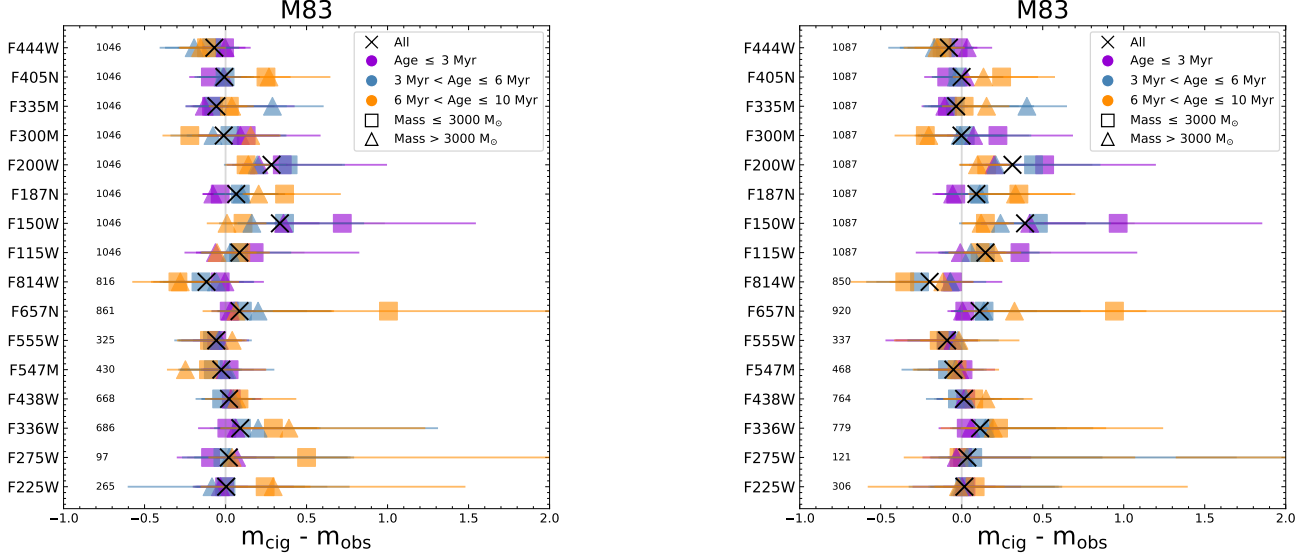

Figure 13. Same as the top right panel of Figure 6, but adopting radii of 4 (∼3.6 pc, left) and 6 pixels (∼5.5 pc, right) for the aperture photometry measurements.

Appendix C
Residual Analysis of the YSC Populations in M83,
NGC 628 and 4449

In Section 5.2, we discussed the presence of the NIR excess in the sample of optically selected YSCs in M51, probing that the excess is less evident for these objects compared to the eYSCI population (see Figure 8). Here, we extend the same analysis to the other three galaxies. The results, shown in Figure 14, confirm the trend observed for M51.
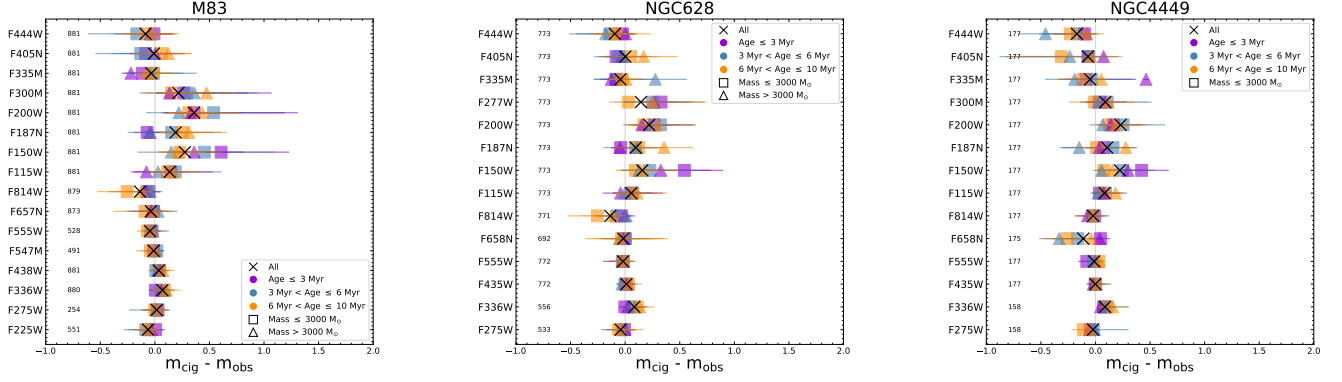

Figure 14. Same as Figure 8, but for the YSC populations in M83 (left), NGC 628 (center), NGC 4449 (right).

Appendix D
SLUG Libraries for 0.4 Solar Metallicity

With a metallicity of $12 + \log(O/H) = 8.26$ and an irregular morphology, NGC 4449 differs from the other three spiral galaxies analyzed in this paper. Consequently, the slug analysis presented in Section 5.4 (Figure 9) requires a slightly modified approach. To account for this, we generate simulated slug cluster libraries using stellar and nebular models with a fixed metallicity of $0.4 Z_\odot$.

The results, shown in Figure 15, indicate that the color differences observed at this lower metallicity are consistent with those seen in Figure 9.
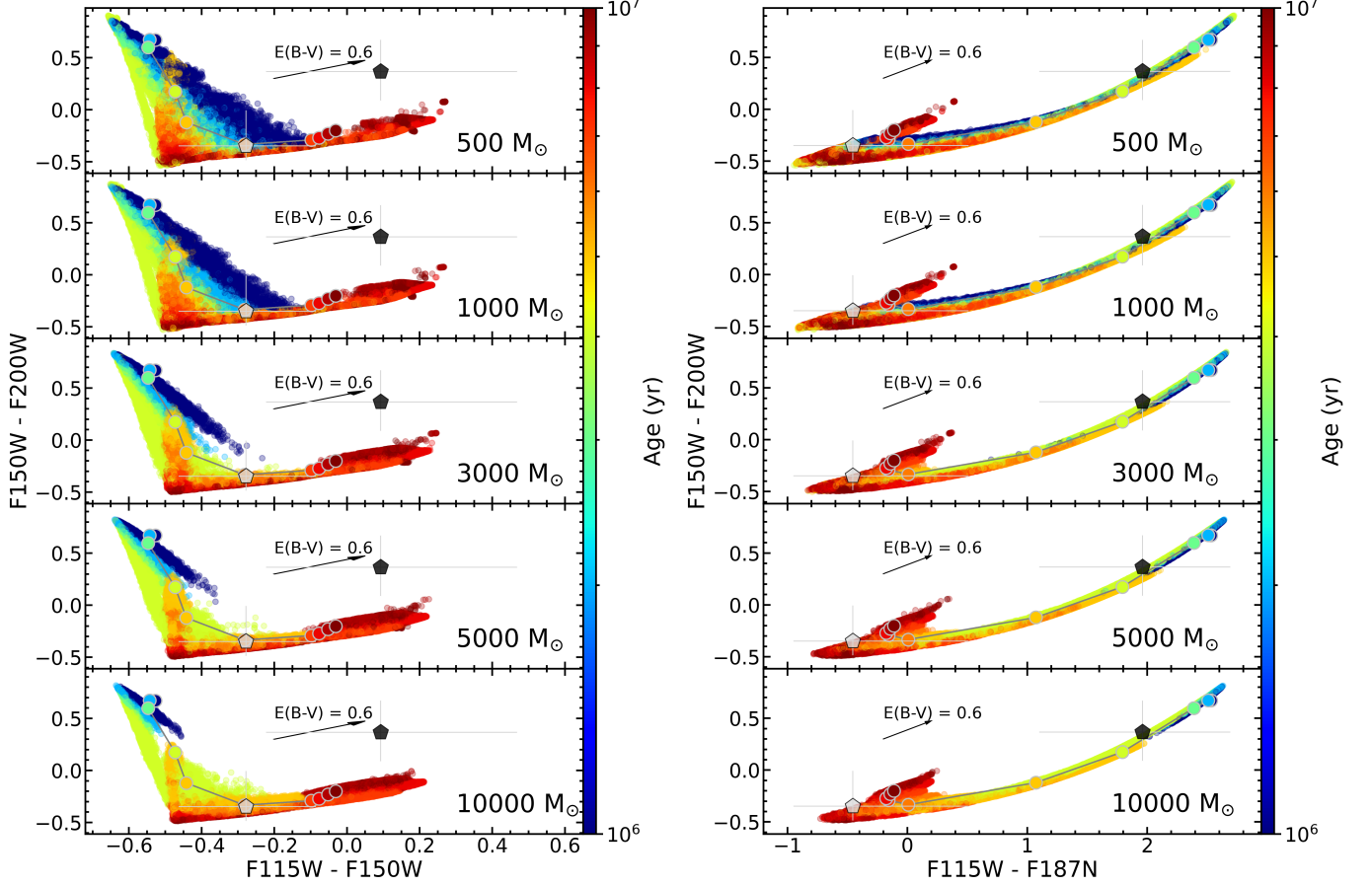

Figure 15. Same as Figure 9, but with adopted metallicity $Z = 0.4\,Z_\odot$. Black and gray pentagons represent the eYSCI and optically identified YSC younger than 10 Myr and with a fitted $E(B-V) < 0.1$ populations in NGC 4449, respectively.

ORCID iDs

Alex Pedrini https://orcid.org/0000-0002-8222-8986
Angela Adamo https://orcid.org/0000-0002-8192-8091
Arjan Bik https://orcid.org/0000-0001-8068-0891
Daniela Calzetti https://orcid.org/0000-0002-5189-8004
Sean T. Linden https://orcid.org/0000-0002-1000-6081
Benjamin Gregg https://orcid.org/0000-0003-4910-8939
Varun Bajaj https://orcid.org/0009-0008-4009-3391
Jenna E. Ryon https://orcid.org/0000-0002-2918-7417
Anne S. M. Buckner https://orcid.org/0000-0002-1832-8229
Giacomo Bortolini https://orcid.org/0009-0003-6182-8928
Michele Cignoni https://orcid.org/0000-0001-6291-6813
Matteo Correnti https://orcid.org/0000-0001-6464-3257
Ana Duarte-Cabral https://orcid.org/0000-0002-5259-4774
Bruce G. Elmegreen https://orcid.org/0000-0002-1723-6330
Helena Faustino Vieira https://orcid.org/0000-0002-2199-0977
John S. Gallagher https://orcid.org/0000-0001-8608-0408
Kathryn Grasha https://orcid.org/0000-0002-3247-5321
Kelsey E. Johnson https://orcid.org/0000-0001-8348-2671
Mark R. Krumholz https://orcid.org/0000-0003-3893-854X
Drew Lapeer https://orcid.org/0009-0009-5509-4706
Thomas S.-Y. Lai https://orcid.org/0000-0001-8490-6632
Matteo Messa https://orcid.org/0000-0003-1427-2456
Göran Östlin https://orcid.org/0000-0002-3005-1349
Linn Roos https://orcid.org/0009-0002-2481-2217
Linda J. Smith https://orcid.org/0000-0002-0806-168X
Monica Tosi https://orcid.org/0000-0002-0986-4759

References

Adamo, A., Ryon, J. E., Messa, M., et al. 2017, ApJ, 841, 131
Adamo, A., Zeidler, P., Kruijssen, J. M. D., et al. 2020, SSRv, 216, 69
Barbary, K. 2016, JOSS, 1, 58
Bastian, N., Adamo, A., Schirmer, M., et al. 2014, MNRAS, 444, 3829
Berg, D. A., Pogge, R. W., Skillman, E. D., et al. 2020, ApJ, 893, 96
Boquien, M., Burgarella, D., Roehlly, Y., et al. 2019, A&A, 622, A103
Bresolin, F., Kudritzki, R.-P., Urbaneja, M. A., et al. 2016, ApJ, 830, 64
Bruzual, G., & Charlot, S. 2003, MNRAS, 344, 1000
Calzetti, D. 2013, in Secular Evolution of Galaxies, ed. J. Falcón-Barroso & J. H. Knapen, 419 (Cambridge: Cambridge Univ. Press)
Calzetti, D., Adamo, A., Linden, S. T., et al. 2024, ApJ, 971, 118
Calzetti, D., Armus, L., Bohlin, R. C., et al. 2000, ApJ, 533, 682
Calzetti, D., Chandar, R., Lee, J. C., et al. 2010, ApJL, 719, L158
Calzetti, D., Lee, J. C., Sabbi, E., et al. 2015, AJ, 149, 51
Cardelli, J. A., Clayton, G. C., & Mathis, J. S. 1989, ApJ, 345, 245
Cerviño, M., & Luridiana, V. 2004, A&A, 413, 145
Chabrier, G. 2003, PASP, 115, 763
Chandar, R., Whitmore, B. C., Calzetti, D., & O'Connell, R. 2014, ApJ, 787, 17
Chastenet, J., Sandstrom, K., Chiang, I.-D., et al. 2019, ApJ, 876, 62
Chown, R., Okada, Y., Peeters, E., et al. 2025, A&A, 698, A86
Crowther, P. A., Hadfield, L. J., Clark, J. S., Negueruela, I., & Vacca, W. D. 2006, MNRAS, 372, 1407
Csörnyei, G., Anderson, R. I., Vogl, C., et al. 2023, A&A, 678, A44
da Silva, R. L., Fumagalli, M., & Krumholz, M. 2012, ApJ, 745, 145
Dale, D. A., Helou, G., Magdis, G. E., et al. 2014, ApJ, 784, 83
De Marchi, G., Giardino, G., Biazzo, K., et al. 2024, ApJ, 977, 214
Dobbs, C. 2023, FrASS, 10, 1272771
Dotter, A. 2016, ApJS, 222, 8
Draine, B. T., Aniano, G., Krause, O., et al. 2014, ApJ, 780, 172
Draine, B. T., Dale, D. A., Bendo, G., et al. 2007, ApJ, 663, 866
Draine, B. T., & Li, A. 2007, ApJ, 657, 810
Eiroa, C., Garzón, F., Alberdi, A., et al. 2001, A&A, 365, 110
Elmegreen, B. G., & Efremov, Y. N. 1996, ApJ, 466, 802
Fahrion, K., & De Marchi, G. 2023, A&A, 671, L14
Fensch, J., Duc, P.-A., Boquien, M., et al. 2019, A&A, 628, A60
Ferland, G. J., Porter, R. L., van Hoof, P. A. M., et al. 2013, RMxAA, 49, 137
Gaia Collaboration, Vallenari, A., Brown, A. G. A., et al. 2023, A&A, 674, A1

Gregg, B., Calzetti, D., Adamo, A., et al. 2024, ApJ, 971, 115
Gregg, B., Calzetti, D., Adamo, A., et al. 2025, ApJ, submitted
Gutermuth, R. A., Pipher, J. L., Megeath, S. T., et al. 2011, ApJ, 739, 84
Haemmerlé, L., Eggenberger, P., Ekström, S., et al. 2019, A&A, 624, A137
Heyer, M. H., Ladd, E. F., Myers, P. C., & Campbell, B. 1990, AJ, 99, 1585
Hillenbrand, L. A., Strom, S. E., Calvet, N., et al. 1998, AJ, 116, 1816
Hollenbach, D. J., & Tielens, A. G. G. M. 1999, RvMP, 71, 173
Hosokawa, T., Offner, S. S. R., & Krumholz, M. R. 2011, ApJ, 738, 140
Hunter, T. R., Brogan, C. L., MacLeod, G., et al. 2017, ApJL, 837, L29
Indebetouw, R., Whitney, B. A., Johnson, K. E., & Wood, K. 2006, ApJ, 636, 362
Inoue, A. K. 2011, MNRAS, 415, 2920
Jensen, S. S., & Haugbølle, T. 2018, MNRAS, 474, 1176
Johnson, K. E., Indebetouw, R., & Pisano, D. J. 2003, AJ, 126, 101
Johnson, K. E., Indebetouw, R., Watson, C., & Kobulnicky, H. A. 2004, AJ, 128, 610
Johnson, K. E., Leroy, A. K., Indebetouw, R., et al. 2015, ApJ, 806, 35
Johnson, L. C., Seth, A. C., Dalcanton, J. J., et al. 2016, ApJ, 827, 33
Kenyon, S. J., & Hartmann, L. 1995, ApJS, 101, 117
Kim, J.-G., Kim, W.-T., & Ostriker, E. C. 2018, ApJ, 859, 68
Knutas, A., Adamo, A., Pedrini, A., et al. 2025, arXiv:2505.08874
Kruijssen, J. M. D. 2015, MNRAS, 454, 1658
Krumholz, M. R., Fumagalli, M., da Silva, R. L., Rendahl, T., & Parra, J. 2015, MNRAS, 452, 1447
Krumholz, M. R., McKee, C. F., & Bland-Hawthorn, J. 2019, ARA&A, 57, 227
Lada, C. J. 1987, in IAU Symp. 115, Star Forming Regions, ed. M. Peimbert & J. Jugaku (Cambridge: Cambridge Univ. Press), 1
Leitherer, C., Schaerer, D., Goldader, J. D., et al. 1999, ApJS, 123, 3
Leroy, A. K., Schinnerer, E., Hughes, A., et al. 2021, ApJS, 257, 43
Levy, R. C., Bolatto, A. D., Mayya, D., et al. 2024, ApJL, 973, L55
Linden, S. T., Lai, T., Evans, A. S., et al. 2024, ApJL, 974, L27
Maíz Apellániz, J. 2009, ApJ, 699, 1938
Maschmann, D., Lee, J. C., Thilker, D. A., et al. 2024, ApJS, 273, 14
Matsukoba, R., Vorobyov, E. I., & Hosokawa, T. 2024, arXiv:2404.05805
Mauerhan, J. C., Van Dyk, S. D., & Morris, P. W. 2009, PASP, 121, 591
Mauerhan, J. C., Van Dyk, S. D., & Morris, P. W. 2011, AJ, 142, 40
Meilland, A., Millour, F., Kanaan, S., et al. 2012, A&A, 538, A110
Menon, S. H., Federrath, C., & Krumholz, M. R. 2022, MNRAS, 517, 1313
Messa, M., Adamo, A., Östlin, G., et al. 2018, MNRAS, 473, 996
Messa, M., Calzetti, D., Adamo, A., et al. 2021, ApJ, 909, 121
Pathak, D., Leroy, A., Thompson, T., et al. 2025, ApJ, 982, 140
Peck, M. L. 1980, ApJ, 238, 79
Pedrini, A., Adamo, A., Calzetti, D., et al. 2024, ApJ, 971, 32
Peeters, E., Habart, E., Berne, O., et al. 2024, A&A, 685, A74
Pilyugin, L. S., Grebel, E. K., & Zinchenko, I. A. 2015, MNRAS, 450, 3254
Richert, A. J. W., Feigelson, E. D., Getman, K. V., & Kuhn, M. A. 2015, ApJ, 811, 10
Richert, A. J. W., Getman, K. V., Feigelson, E. D., et al. 2018, MNRAS, 477, 5191
Rigby, J., Perrin, M., McElwain, M., et al. 2023, PASP, 135, 048001
Rodríguez, M. J., Lee, J. C., Whitmore, B. C., et al. 2023, ApJL, 944, L26
Sabbi, E., Calzetti, D., Ubeda, L., et al. 2018, ApJS, 235, 23
Schlafly, E. F., & Finkbeiner, D. P. 2011, ApJ, 737, 103
Schroetter, I., Berné, O., Joblin, C., et al. 2024, A&A, 685, A78
Stanway, E. R., & Eldridge, J. J. 2023, MNRAS, 522, 4430
Sun, J., He, H., Batschkun, K., et al. 2024, ApJ, 967, 133
Tully, R. B., Courtois, H. M., Dolphin, A. E., et al. 2013, AJ, 146, 86
Tully, R. B., Rizzi, L., Shaya, E. J., et al. 2009, AJ, 138, 323
Turner, J. A., Dale, D. A., Lee, J. C., et al. 2021, MNRAS, 502, 1366
Turner, J. A., Dale, D. A., Lilly, J., et al. 2022, MNRAS, 516, 4612
Whelan, D. G., Johnson, K. E., Whitney, B. A., Indebetouw, R., & Wood, K. 2011, ApJ, 729, 111
Whitmore, B. C., Chandar, R., Kim, H., et al. 2011, ApJ, 729, 78
Whitmore, B. C., Chandar, R., Lee, J., et al. 2020, ApJ, 889, 154
Whitmore, B. C., Chandar, R., Lee, J. C., et al. 2025, ApJ, 982, 50
Whitmore, B. C., Chandar, R., Rodríguez, M. J., et al. 2023, ApJL, 944, L14
Winter, A. J., & Haworth, T. J. 2022, EPJP, 137, 1132
Wofford, A., Charlot, S., Bruzual, G., et al. 2016, MNRAS, 457, 4296
Yang, G., Boquien, M., Buat, V., et al. 2020, MNRAS, 491, 740
Yasui, C., Kobayashi, N., Tokunaga, A. T., Saito, M., & Tokoku, C. 2010, ApJL, 723, L113
Zackrisson, E., Rydberg, C.-E., Schaerer, D., Östlin, G., & Tuli, M. 2011, ApJ, 740, 13
Zucker, C., Alves, J., Goodman, A., Meingast, S., & Galli, P. 2023, in ASP Conf. Ser. 534, Protostars and Planets VII, ed. S. Inutsuka et al. (San Francisco, CA: ASP), 43